DEVELOPMENT OF A LARGE AREA SILICON PHOTOMULTIPLIER ARRAY FOR LIGHT DETECTION IN LIQUID XENON

MASTER'S THESIS IN PHYSICS

AKO JAMIL
November 10, 2017

FRIEDRICH-ALEXANDER UNIVERSITY
ERLANGEN-NÜRNBERG

SUPERVISOR:
PROF. DR. GISELA ANTON

PROJECT PERFORMED AT
STANFORD UNIVERSITY
IN COOPERATION WITH
PROF. DR. GIORGIO GRATTA

Abstract

Previous experiments that searched for ultra rare events, like dark matter or the neutrinoless double beta decay, have been mostly using conventional Photomultiplier Tubes to detect scintillation light. Most recently, Silicon Photomultipliers have proven to be a mature enough technology and became available for a broad spectrum of applications. Nowadays, they even reach a reasonable detection efficiency for VUV light in experiments that use noble liquids, like argon or xenon. The nEXO experiment, a future multi-tonne liquid xenon time projection chamber, will use Silicon Photomultiplier on a large scale for the detection of VUV scintillation light, which comes with a significant improvement in light collection, and hence energy resolution. Together with nEXO's enhanced self-shielding capabilities and other improvements, a 1% (σ_E/E) energy resolution at the Q-value of 2458 keV will be reached, which will allow nEXO to probe a wide range of the inverted neutrino mass hierarchy and set the most stringent results on the neutrino mass ordering. Current projections indicate that nEXO will have, among double beta decay experiments that use ^{136}Xe, the largest discovery potential with a probability of larger than 60% for the inverted neutrino mass hierarchy after 5 years of data taking. This thesis comprises the study of the Silicon Photomultiplier performance and the development of a light readout module based on Silicon Photomultipliers.

Contents

Chapter 1

Introduction

Our current knowledge about the origin of mass is derived from the Brout-Englert-Higgs mechanism, that uses the formalism of spontaneous symmetry breaking to elegantly describe how all elementary particles in the Standard Model of Particle Physics acquire their mass [1, 2]. This theory was proven by the independent discovery of a predicted light Higgs-like boson by the CMS and ATLAS collaborations at the Large Hadron Collider at CERN and was also awarded the Nobel Prize in Physics in 2013 [3, 4]. The only exemption to this theory is the neutrino. Until two decades ago, neutrinos were unlike any other fermion assumed to be massless, which required a so-called "unnatural" fine-tuning of the Standard Model. However, studies of neutrino oscillations of solar and atmospheric neutrinos, reactor neutrinos, and neutrino beams, have shown that neutrinos indeed have a non-zero mass [5–8]. This led to the current picture of distinct neutrino mass and flavor eigenstates, that can be mixed according to the Pontecorvo–Maki–Nakagawa–Sakata matrix [9]. The Nobel Prize in Physics in 2016 honors this discovery.

Furthermore, below the electroweak symmetry breaking energy of 246 GeV all charged fermions in the Standard Model can be described as Dirac particles [10]. This implies a distinction of a particle and its corresponding anti-particle, which is given by the sign of the electric charge that both carry. Since neutrinos do not carry electric charge, the only distinction of neutrino and anti-neutrino is based on their possible interaction processes. This origins in the CP-parity violation and the fact that the weak interaction couples to left-handed particles and right-handed anti-particles only. In this context, handedness corresponds to the chirality eigenvalue.

The above gives rise to the question whether the neutrino can be described within a different framework, assuming a Majorana nature, e.g. that the neutrino is its own anti-particle [11]. For instance, by introducing a new Majorana mass term into the Standard Model Lagrangian the huge discrepancy between the mass scale in the quark and charged lepton sector and the neutrinos can be easily resolved [12, 13]. Out of many possible ways to prove that neutrinos are Majorana fermions, the neutrinoless double beta decay is yet the experimentally most feasible one [12, 14]. This is a hypothetical decay, where, due to energy conservation arguments for some nuclei, two beta decays have to take place simultaneously and no neutrinos are emitted.

The nEXO collaboration plans to build a 5 tonne single sided and cylindrical single phase time projection chamber (TPC) filled with liquid xenon and an enrichment of about 90% in ^{136}Xe to search for the neutrinoless double beta decay of ^{136}Xe. The decay leaves, due to the absence of neutrinos in the final state, a distinct signal with the sum energy of the two outgoing electrons, centered at the Q-value of the decay. nEXO will use Silicon Photomultipliers (SiPMs) on a large scale and at cryogenic temperatures for the detection of vacuum ultra-violet (VUV) scintillation light at 178 nm [15]. The lateral surface will be covered with SiPMs, making up a total photo-sensitive surface area of about 4 m^2. This unique design requires placing the photo detectors behind the field shaping rings in the presence of a high electric field. The purpose is to maximize the

light collection efficiency, which ultimately results in a significant improvement of the energy resolution. To further increase the light collection, highly reflective materials in the VUV range are considered as a coating for most components.

This thesis presents recent work on characterizing SiPMs and the effort that has been put into the development of a prototype of a nEXO light readout system. The second chapter starts with a brief introduction to neutrino physics in general, with a focus on the neutrinoless double beta decay in particular. A description of the conceptual design of the nEXO detector follows in the third chapter, with an emphasis on the light collection. The fourth chapter focuses on the vacuum setup at Stanford University that was used for the characterization of SiPMs in the VUV range and evaluates the most recent results of detection efficiencies and the overall performance of these devices. The last two chapters present the prototyping of a large area SiPM array for the light detection in liquid xenon and the corresponding light simulations for the Stanford setup, that were done with the ultra fast Monte-Carlo-based Chroma software.

Chapter 2

Massive Neutrinos and the Neutrinoless Double Beta Decay

This chapter introduces the current knowledge about neutrinos, that is important for understanding the neutrinoless double beta decay ($0\nu\beta\beta$). It starts with a summary of the discovery of neutrino oscillations and continues with the necessity of massive neutrinos for a Majorana nature of neutrinos, which means that they are their own anti-particle. A brief insight into the consequences for the Standard Model and physics beyond the Standard Model will be given. The last part focuses on possible detection techniques, the current best limits and various challenges that $0\nu\beta\beta$ experiments are facing.

2.1 Neutrino Oscillations and their Consequences

The Standard Model of Particle Physics describes neutrinos as massless leptons, that do not carry electric charge. Experimentally, we know that only three light active neutrinos exist, where light means that $m_\nu < m_Z/2$ with m_ν and m_Z being the masses of the neutrino and the Z-Boson, respectively. They are paired with their corresponding charged lepton in weak iso-doublets and are Dirac particles, e.g. they have their distinct anti-particle. They do not participate in the strong or electromagnetic interaction, and hence are only observable through the weak interaction and gravitation.

However, neutrino oscillations experiments have not only shown that neutrinos are indeed massive, but also imply that the neutrino states that participate in the weak interaction, so called *flavor eigenstates*, are different from the neutrino *mass eigenstates*, that are responsible for the free particle evolution. In general, this means that the three neutrino weak eigenstates can be expressed as a linear combination of the mass eigenstates:

$$|\nu_i\rangle = \sum_j U_{ij}^* |\nu_j\rangle \tag{2.1}$$

where U_{ij}^* denotes the 3×3 unitary neutrino mixing matrix with $U_{ij}^* \neq \mathbb{1}_3$. A typical parametrization of the mixing matrix uses three mixing angles θ_{12}, θ_{13}, θ_{23} and three phases δ, α_{21}, α_{31}. In the case of a Dirac neutrino, the so called Dirac phase δ will be observable and could be possibly CP violating. All three mixing angles have been measured and are known to be non-zero. However, in terms of masses, neutrino oscillation experiments can only provide information on mass square differences $\Delta_{ij} = m_i^2 - m_j^2$, but cannot make any statement about the absolute mass scale of neutrinos. Hence, it is not yet clear which mass eigenstate m_i is the lightest, as shown in figure 2.1. Additional

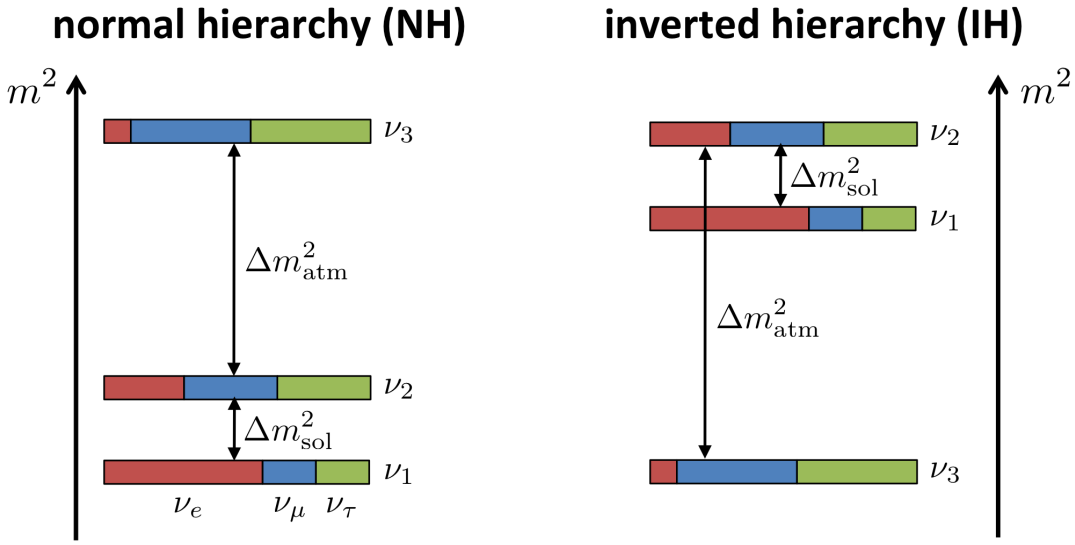

Figure 2.1: Possible ordering schemes of the neutrino mass eigenstates. The left one is the so-called "normal hierarchy", whereas the right one is referred to as the "inverted hierarchy". The colors encode the relative contribution of each neutrino flavor eigenstate to the neutrino mass eigenstate, with red for ν_e, blue for ν_μ and green for ν_τ.

information from other non-oscillation experiments, like measurements of the β-decay endpoint, cosmological observations or the neutrinoless double beta decay, is needed in order to determine the mass ordering.

2.2 Majorana Neutrinos and Physics Beyond the Standard Model

The mere fact that neutrinos have a non-zero mass is already in contradiction to the Standard Model, but it allows to search for even more physics beyond the Standard Model since it enables processes that would have been impossible otherwise.

The neutrinoless double beta decay ($0\nu\beta\beta$) is such a process. It is a second order weak process in which two protons of a nucleus with atomic number Z transform into two neutrons and two electrons are emitted. No neutrinos are present in the final state of this decay, as shown in the Feynman diagram on the right side in figure 2.2. There are a couple of premises in order for $0\nu\beta\beta$ to happen:

- The standard β-decay to the $Z+1$ nuclide is either energetically forbidden or strongly suppressed, which makes the neutrino-accompanied double beta decay ($2\nu\beta\beta$) the more favorable decay channel. The Feynman diagram of this decay is shown on the left side of figure 2.2. This is true for at least 35 naturally occurring isotopes, including ^{136}Xe, which will be discussed in more detail in chapter 3.

- In contrast to all other fermions in the Standard Model, which are Dirac fermions, neutrinos have to be Majorana fermions, e.g. that the neutrino is its own anti-particle. Since neutrinos are electrically neutral and intrinsically parity violating it is possible that this is the case. Therefore, the left-handed helicity component would be referred to as neutrino ν, whereas the right-handed helicity component would be the anti-neutrino $\bar{\nu}$.

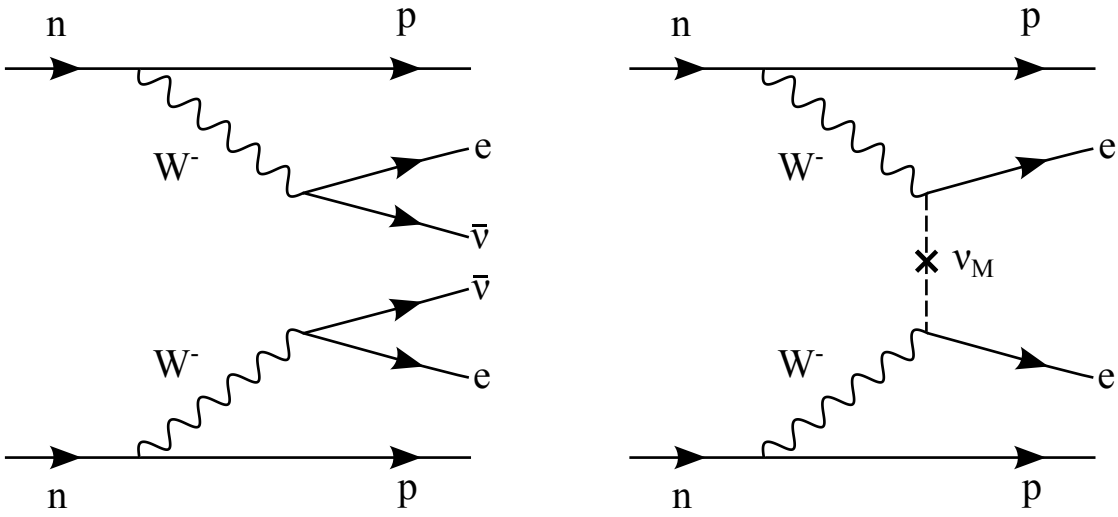

Figure 2.2: Feynman diagram of the neutrino accompanied (left) and neutrinoless (right) double beta decay. The standard mechanism without the requirement of new particles or interactions beyond the Standard Model is shown for the neutrinoless case. This version is based on the exchange of a light Majorana neutrino.

- Neutrinos need to have a non-zero mass. If one would read the Feynman diagram in figure 2.2 from the bottom to the top, the following would need to happen. In order for the right-handed anti-neutrino, that is for instance emitted at the bottom vertex, to be absorbed at the top vertex a change in helicity is inevitable. Since for massless particles the helicity and chirality eigenvalues are identical and conserved in all inertial frames, the $0\nu\beta\beta$ would not be possible. However, for a particle with finite mass an inertial frame of reference can be found where the helicity eigenvalue is flipped, and hence the anti-neutrino can be absorbed at the other vertex as a left-handed neutrino due to its Majorana nature.

- The existence of the $0\nu\beta\beta$ would require lepton number conservation to be violated. The initial state of the decay has a lepton number of $L = 0$, whereas the final state has $L = 2$, because of the absence of the anti-neutrinos which would normally compensate for the surplus. Unlike other conserved quantities that are fundamental to physics, like energy, lepton number conservation has just empirically grown.

For the sake of simplicity, only the standard mechanism is mentioned. Moreover, independently of the actual process enabling the neutrinoless double beta decay, the Schechter-Valle-Theorem ensures that an observation would prove the Majorana nature of neutrinos [16]. In any case, the observation of this process has discovery potential of new physics on many levels, as described above.

2.3 Experimental Approach

The event signature of interest is the sum energy of both outgoing electrons of the decay. In the neutrino-accompanied case the sum energy of both electrons is a broad spectrum ranging all the way up to the Q-value of the decay. However, without neutrinos all the energy of the decay is transferred to the electrons and, hence leaves a narrow peak centered at the Q-value of the decay, which is the amount of energy released in the

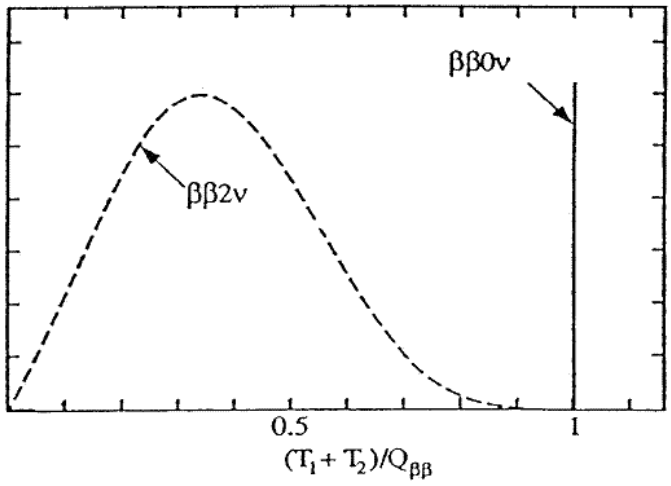

Figure 2.3: Energy spectrum of both possible double beta decay modes. The broad and continues spectrum, shown as dashed lines, corresponds to the $2\nu\beta\beta$ where the two electrons carry only part of the total decay energy. In the $0\nu\beta\beta$ case the two electrons carry all the decay energy which leaves a narrow peak at the Q-value. Finite energy resolution broadens the peak.

Experiment	**Mass [tonne]**	$\mathbf{T_{1/2}}$ **[10^{25} yrs]**	$\mathbf{m_{\beta\beta}}$ **[eV]**	**ROI [eV]**
EXO-200	0.16	1.1	$0.19 - 0.47$	150 ($\pm 2\sigma$)
KamLAND-Zen	0.32	11	$0.06 - 0.15$	400
GERDA	0.018	2.1	$0.24 - 0.41$	5 (FWHM)
CUORE-0	0.013	0.4	$0.26 - 0.71$	5.1 (FWHM)

Table 2.1: Comparison of currently leading $0\nu\beta\beta$ decay experiments. The numbers stated for $T^{0\nu}_{1/2}$ and $m_{\beta\beta}$ are with a 90% C.L. [12].

decay. For the $0\nu\beta\beta$ of ^{136}Xe the Q-value is at 2458 keV. Both scenarios are shown in figure 2.3. Because of the finite energy resolution a true signal will be a broadened peak at the Q-value. One main challenge for future tonne-scale experiments is the intrinsic background from $2\nu\beta\beta$ events, that every experiment will have to face at a point. In order to be able to discriminate those two modes a very good energy resolution is crucial to make a discovery. In the case of no observation of $0\nu\beta\beta$, a new lower limit on the half-life can be extracted and, under the assumption that the exchange of a light Majorana neutrino is the dominant process, can be expressed as:

$$\left(T^{0\nu}_{1/2}\right)^{-1} = G_{0\nu}(Q_{\beta\beta}, Z) \cdot |M_{0\nu}|^2 \cdot m^2_{\beta\beta} \tag{2.2}$$

which is linked to the effective Majorana neutrino mass $m_{\beta\beta}$. $G_{0\nu}(Q_{\beta\beta}, Z)$ is the so-called phase-space factor that depends on the total energy and the details of the underlying kinematics of the decay, and can be calculated exactly. Furthermore, $|M_{0\nu}|$ is the nuclear matrix element, that requires various approximations to be calculated and is hence subject to large theoretical uncertainties [17]. The last term denotes the effective Majorana neutrino mass

$$m_{\beta\beta} = \left| \sum_{i=1}^{3} m_i U^2_{ei} \right| \tag{2.3}$$

where m_i are the neutrino mass eigenstates and U_{ei} are elements of the neutrino mixing matrix.

The sensitivity of a double beta decay experiment depends on various different parameters, including the choice among possible $\beta\beta$ isotopes, detector mass, signal readout, signal discrimination and others. To maximize the sensitivity on the half-life of a specific decay, i.e. the decay of ^{136}Xe, or, more generally, to the effective Majorana neutrino mass, the following dependencies need to be accounted for

$$m_{\beta\beta} \sim \sqrt{\frac{1}{\epsilon}} \cdot \left(\frac{c \cdot \Delta E}{M \cdot t} \right)^{1/4} \tag{2.4}$$

with the signal detection efficiency ϵ, the background rate c in counts/(keV $\cdot$ kg $\cdot$ yr), the overall exposure $M \cdot t$ and the energy window ΔE of interest around the Q-value. Table 2.1 summarizes the currently leading experiments that search for $0\nu\beta\beta$ of ^{130}Te, ^{76}Ge and ^{136}Ge. It shows their detector mass, their current best half-life sensitivity, their limit on the effective Majorana mass and their energy resolution at the Q-value. Notably, no experiment has reached the tonne scale yet.

Chapter 3

The nEXO Experiment

This chapter will introduce the details of the future nEXO experiment that will search for $0\nu\beta\beta$ of the ^{136}Xe isotope. The conceptual design of the liquid xenon time projection chamber, that is influenced by the experience from the successful predecessor EXO-200, will be described in the first section. The second section will follow up with the functionality of the time projection chamber, its benefits and the actual implementation in nEXO. The last section will discuss the light readout with SiPMs in nEXO in more detail and will highlight the improvements compared to other technologies like Photomultiplier Tubes or Avalanche Photodiodes.

3.1 Conceptual Detector Design

The nEXO experiment will be a time projection chamber (TPC) filled with 5000 kg of liquid xenon with an enrichment of about 90% in ^{136}Xe. The conceptual design is shown in figure 3.1, which has adapted some key feature of its predecessor EXO-200. The most inner part is the copper cryostat, that will later contain the liquid xenon (LXe), and will be made out of ultra clean Aurubis copper [18], that was proven by the EXO-200 collaboration to be the cleanest available copper world wide. In this context cleanness means radio pureness. Similarly, the TPC will be a monolithic, single phase detector, but much larger with 1.3 m in diameter and height, compared to 40 cm in diameter and 20 cm height of one of the EXO-200 TPCs'. The copper cryostat will be surrounded by the cooling fluid HFE-7000 [19], which provides both, good thermal uniformity and shielding from external radiation. The most outer spherical cryostat maintains an insulation vacuum to thermally isolate the HFE cryostat from the environment. The whole construction is placed inside a large water tank, where Photomultiplier Tubes (PMTs) will be instrumented, that serve as a muon veto system and adds additional shielding from any radiation from the underground material.

EXO-200 has powerfully demonstrated that a detector where the medium is the decaying and detecting material at the same time has huge background rejection capabil-

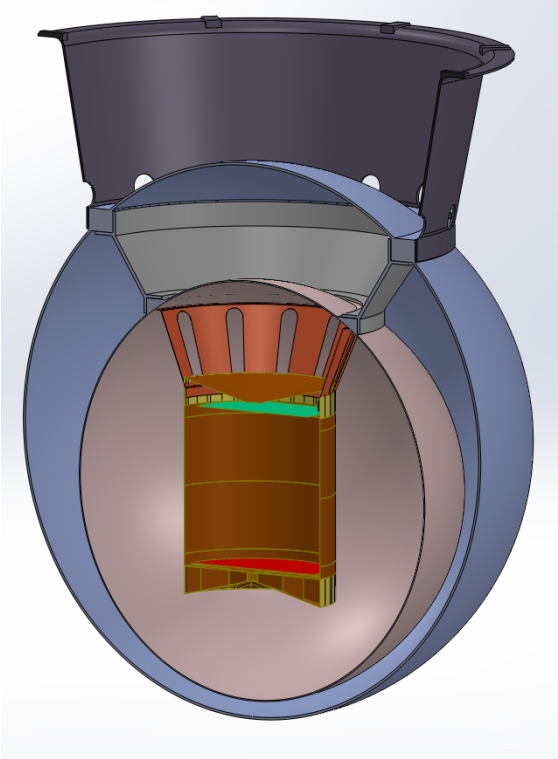

Figure 3.1: Conceptual design of the nEXO detector. It consists of an inner copper TPC that is surrounded by the cooling fluid HFE. The red surface represents the cathode, that will be placed at one of the ends of the TPC, and the green surface marks the charge readout tiles. The HFE cryostat is contained within an insulation vacuum to thermally isolate it from the outside. The whole construction will be placed inside a huge water tank, that will be instrumented with photomultiplier tubes to discriminate cosmic rays. nEXO will most likely be deployed deep underground at SNOLAB.

ities. This is due to the excellent self shielding capabilities of xenon. For instance, the attenuation length of a high energetic γ-ray originating from the ^{232}Th decay chain with about 2.6 MeV is about 8.5 cm. Therefore, by fiducializing the detector, which means considering only a small volume in the inner part of the detector, most of the external and surface background can be rejected. The smaller the fiducial volume, the cleaner the detector will be from background contaminations. To further improve and benefit from the purity of the center region, nEXO will place the cathode at one of the ends of the TPC, unlike in EXO-200 where the cathode is in the center of the detector.

The larger drift length, that may cause higher losses of electrons, will need to be compensated with higher chemical purity of the xenon to avoid absorption of electrons by electro-negative impurities such as oxygen. This will be achievable by a higher xenon recirculation flow rate, that will need to be maintained all the time. An additional challenge with a larger detector is the larger electric field that needs to be applied in order to keep a stable 376 V/cm drift field throughout the TPC.

In general, xenon makes a good isotope candidate for a $0\nu\beta\beta$ experiment because of the scalability of such an experiment, relatively easy cleaning and high natural abundance of the ^{136}Xe isotope of about 9.8%. Considering the world xenon production of about 30-40 tonnes, which corresponds to about 3-4 tonnes of enriched ^{136}Xe, it still remains a challenge to acquire the planned detector mass of 5000 kg.

Currently, the most likely site for nEXO is in the deep underground laboratory at SNOLAB [20] to prevent cosmic activation of ^{137}Xe.

3.2 The Liquid Xenon Time Projection Chamber

The nEXO detector is designed as a TPC, which allows not only for calorimetry, but also for reconstructing spatial information of an event and a powerful discrimination based on the topology of an event.

The two electrons, that emerge from a $0\nu\beta\beta$ decay, deposit their energy in the detector by either ionizing or exciting surrounding xenon atoms. The typical track length for these electrons in liquid xenon is in the range of a few mm. Both, the ionized Xe^+ and the excited Xe^* will form so-called excimers, that after a cascade of deexcitations produce scintillation light in the VUV range:

$$Xe^* + Xe + Xe \quad \rightarrow \quad Xe_2^* + Xe \quad \rightarrow \quad 2Xe + h\nu + \ldots \tag{3.1}$$

$$Xe^+ + Xe \quad \rightarrow \quad \ldots \quad \rightarrow \quad Xe_2^* + Xe + \ldots \quad \rightarrow \quad 2Xe + h\nu + \ldots \tag{3.2}$$

Typically, the scintillation light has two major components that correspond to the two possible states of the excimer. For liquid xenon the major component in the VUV range is centered around 177.6 nm, whereas the other component is in the infrared region.

An energy deposit E in the detector yields a total number of E/W_{ph} scintillation photons. W_{ph} is the average energy for producing a scintillation photon, which can be expressed as

$$W_{\mathrm{ph}} = W \cdot \frac{N_i}{1 + N_{\mathrm{ex}}} \tag{3.3}$$

with the assumption of no quenching. The value for W_{ph} depends on the ionizing particle or, more generally, on the linear energy transfer, which is how densely electron-ion pairs are produced along the track of ionization. It is 21.6 eV and 17.9 eV for electrons and α-particles, respectively. Another factor that will influence the number of produced

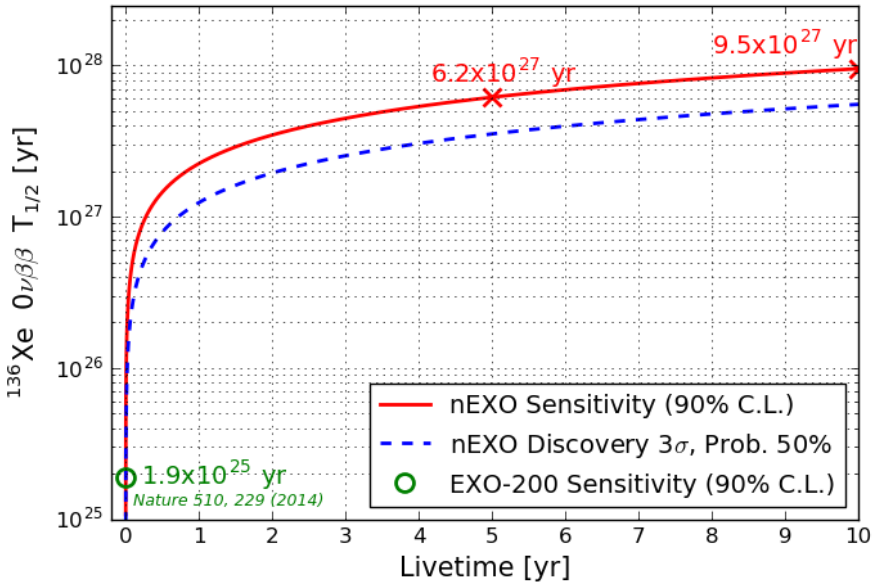

Figure 3.2: Projected sensitivity (red solid line) and 3σ discovery potential (blue dashed line) of nEXO as a function of the livetime of the experiment. The green marker shows the EXO-200 sensitivity of 1.9×10^{25} yr in phase I. In comparison, nEXO will reach a half-life sensitivity of 6.2×10^{27} yr after 5 years of data taking, which is already an improvement of 2 order of magnitude. Another 5 years of data taking will give a final sensitivity of 9.5×10^{27} yrs. All the sensitivities are given on a 90 % C.L.

scintillation photons is the strength of the electric field in the TPC. The higher the drift field is, the less likely a recombination of electron-ion pairs is and, hence the lower the scintillation yield. On the contrary, the number of charge carriers will increase with higher electric field. This results in a strong anti-correlation in the signal strength of the light and charge signal. It turns out that the anti-correlation can be used to achieve a better energy resolution by using the summed signal of both, the light and charge [21].

The scintillation light, that is produced within the TPC, will be basically detected instantaneously by the SiPMs, which will mark a time stamp for this event. The time between the detection of the light signal and the detection of the charge signal gives the position of an event in z-direction. As a comparison, in EXO-200 the anode on which the charge was measured, consisted of two planes of wires that are rotated by 60° with respect to each other. In order to prevent issues that come with a meter-long wire, i.e. the large capacitance and noise or the difficulty in reconstructing multi-site events, a different design is chosen for nEXO. The anode will be an array of smaller-sized square charge tiles, with an edge length of 10 cm each. The current prototype tile consists of an array of pads with a pitch of 3 mm, where 30 pads along the X/Y-axis are connected to a strip, making up a total of sixty strips. Depending on which strips collect the charge the position of an event in x-y-direction can be reconstructed. Hence, the 3 dimensional position can be determined and used for selecting events. As mentioned in chapter 3.1, nEXO benefits from its monolithic design and the good self-shielding capabilities. Together with the 3 dimensional position reconstruction and the advanced energy reconstruction, using light and charge, nEXO aims to have less than 2.9×10^{-5} counts/kg/keV/yr in a 60 keV region of interest (ROI) around the Q-value. This makes nEXO, among other $0\nu\beta\beta$ experiments that use ^{136}Xe, the experiment with the biggest discovery potential [22]. More precisely,

for a fiducial volume of 3.86 tonnes and after 10 years of data taking nEXO will reach a half-life sensitivity of 9.5×10^{27} yr (90 % C.L.), as shown in figure 3.2. This corresponds to a limit between $6 - 17$ meV on the effective Majorana mass $m_{\beta\beta}$.

3.3 Light Detection with Silicon Photomultiplier

One important key to achieve this significant improvement in sensitivity is to use a novel detector for light readout, as the biggest contribution to the overall uncertainty in EXO-200 was from the light channel.

3.3.1 Functionality

The Avalanche Photo Diodes (APDs) in EXO-200 are very similar to pin-photodiodes that are operated in reverse bias mode. This expands the depletion region between the p and n doped regions, resulting in a high electric field there to extract the charge and prevent recombination [23]. In addition, an intrinsic or very faintly doped region is added to further widen the depletion region, which increases the probability for a photon to create an electron-hole-pair via the photo-electric effect. The primary electron will produce additional electron-hole-pairs through collisions with atoms. This charge multiplication process is called avalanche process. As APDs are not operated above breakdown the avalanche will end by itself. A schematic of the topology of a typical APD is shown in figure 3.3.

In a Silicon Photomultiplier (SiPM) many thousand APDs, also called microcell or Single Photon Avalanche Photodiode (SPAD), are connected in parallel. Each cell is operated in Geiger-mode, i.e. the bias voltage is above breakdown. The bias voltage with respect to the breakdown voltage is called over-voltage and is $\Delta V = V_{\text{bias}} - V_{\text{break}}$. Due to the much higher electric field a triggered avalanche will sustain itself and will grow exponentially and would ultimately lead to the destruction of the cell. Typically, a

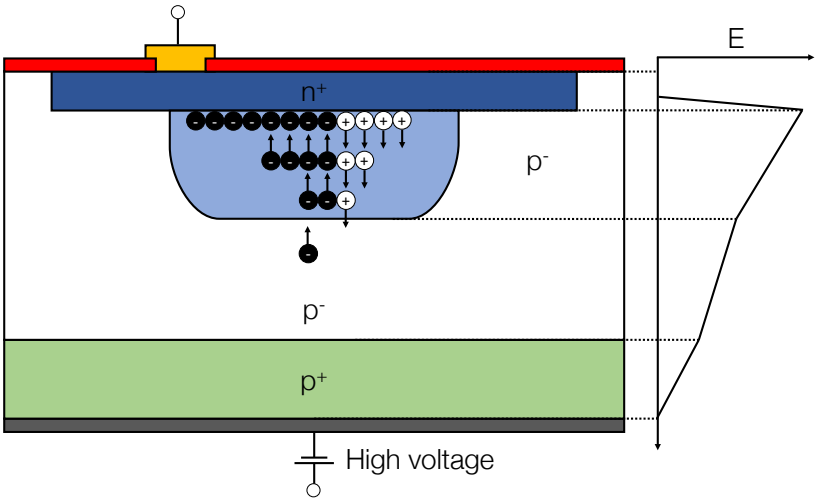

Figure 3.3: Typical structure of an APD that works as a pin-photodiode in reverse bias mode. The qualitative electric field strength inside the diode is shown on the right. An initially created electron will produce additional electron-hole-pairs while drifting towards the n^+ region due to impact ionization of the lattice atoms.

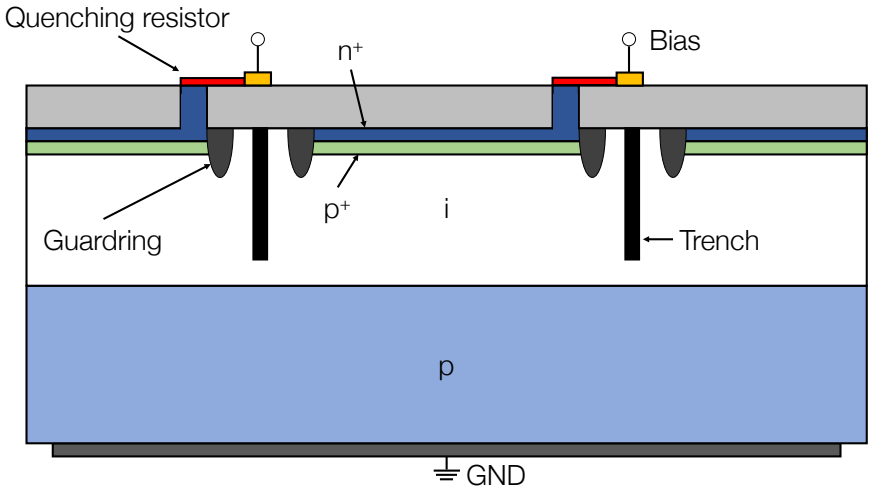

Figure 3.4: Schematic cross-section view of a SiPM shown on a pixel level. Each cell is operating as an individual and independent SPAD, but are ultimately connected together in parallel.

quenching resistor R_{Q} is connected in series to each SPAD that causes a discharge of the cell and stops the avalanche. An equivalent circuit of a SiPM is shown in figure 3.5.

In general, it consists of a capacitor C_{J} that represents the capacitance of the pn-junction to which the quenching resistor R_{Q} is connected in series. In parallel to that, there is the pn-resistivity R_{S} and the effective voltage source V_{BR} that equals the breakdown voltage. The ON and OFF switch presents the state of the pixel, i.e. whether it is ready or triggered. If the cell absorbs a photon, an electron-hole-pair is produced, which will drift to the high electric field region to trigger an avalanche. The switch will immediately close and the capacitor C_{J} will discharge through resistor R_{S} with a time constant $\tau = R_{\mathrm{S}} \cdot C_{\mathrm{J}}$. Consequently, the voltage on C_{J} decreases, hence stopping the multiplication process and the avalanche. The switch turns back to the OFF position and C_{J} will be recharged with a time constant $\tau = R_{\mathrm{Q}} \cdot C_{\mathrm{J}}$. The pixel structure of a SiPM and the high uniformity in gain across all cells allow not only single photon sensitivity, but also single photon resolution. An initially binary information about whether the pixel has fired or not is later transformed into an analog current signal. However, even after the superposition of these analog signals the single photon capability is preserved and can be extracted in the software analysis. Chapter 4 will discuss this in more detail.

During an avalanche various different processes can happen that will contribute to the pure signal response. Figure 3.4, which shows the schematic structure of a SiPM, will be used for illustration. The two main contributions, without going to much into the details, are called optical crosstalk (CT) and afterpulsing (AP). The former takes place when photons, from the recombination of electron and holes in the avalanche, make it to a neighboring pixel. This can happen either directly or via reflection off the top boundary surface due to the mismatch in refractive indexes between silicon and either air, a possible anti-reflective coating or ultimately LXe. Newer versions of SiPMs try to minimize CT by placing trenches between each pixel, that are made out of a material with a large atomic number Z to maximize the photon absorption probability. They are shown as black bulks in figure 3.4. With this method a reduction of CT below 10 % is achievable.

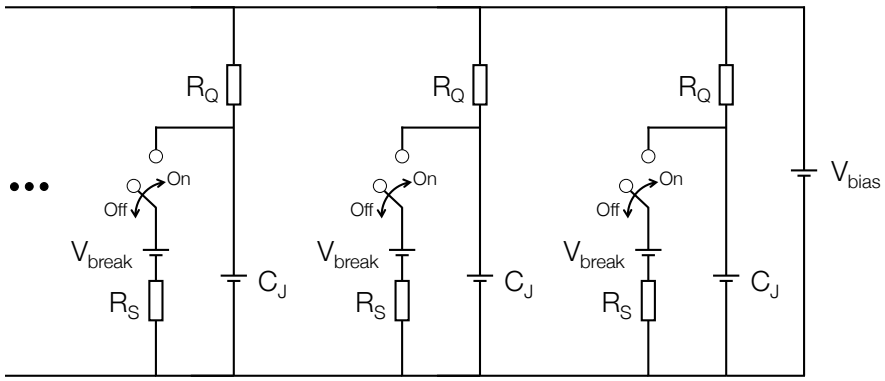

Figure 3.5: Equivalent circuit of a SiPM, showing the structure of the individual cells that are connected in parallel.

The second effect, afterpulsing, is the consequence of an electron being trapped in a lattice defect in the avalanche region. The life time of a trap depends on various parameters of the silicon, i.e. doping type and concentration, but is typically in the order of 10 ns to 100 ns. If the electron is released while the cell is still biased above breakdown, a second avalanche will be triggered. The electron amplification in the additional avalanche depends on the recharge state of the cell. These two combined effects are typically also referred to as correlated avalanches.

3.3.2 Performance Requirements

To meet the prospective sensitivity goals that were derived from detailed simulations and which rely on assumption of various parameters, nEXO has certain requirements that the SiPMs have to fulfill. The most important ones are:

- The Photon-Detection Efficiency (PDE) is the probability to detect a photon that hits the detector and is defined as

$$PDE = QE \cdot P_{\text{trig}} \cdot \epsilon_{\text{geo}} \tag{3.4}$$

  where the quantum efficiency $QE = QE(\lambda)$ is the wavelength dependent probability to absorb a photon and create an electron-hole-pair. $P_{\text{trig}} = P_{\text{trig}}(\Delta V)$ is the probability that an avalanche will be triggered and, hence a measurable signal is created. The trigger probability depends on the OV and typically increases with higher OV due to the higher electric field. The last component is the geometric efficiency ϵ_{geo} which is the ratio of active photo-sensitive area to total surface area of the SiPM. The planned 1% energy resolution at the Q-value requires a minimum of 15 % for the PDE.

- In addition to the intrinsic fluctuations in the production of scintillation light in LXe, the contribution from correlated avalanches further increases the energy resolution. To limit the number of correlated avalanches per parent avalanche within a time window of 1 µs to less than 20% is sufficient.

Table 3.1: Contribution of different sources to the total energy resolution. Compared are different detector designs that either use EXO-200 LAAPDs or SiPMs with different total surface coverage [27].

Source of fluctuations	**APDs**	**SiPMs** ($2\,\mathrm{m}^2$)	**SiPMs** ($4\,\mathrm{m}^2$)
Efficiency	1.3	2.25	1.57
Dark noise	0	0.17	0.12
Correlated avalanche	0	1.14	0.80
Gain	1.4	0.08	0.06
Electronics noise	3.7	0.25	0.18
Total detector induced fluctuations (light only)	4.2	2.5	1.8
LXe intrinsic fluctuations (light only)	5.4	5.4	5.4
Light only resolution	6.84	5.98	5.70
Contribution to combined resolution with charge	1.64	1.04	0.78
LXe intrinsic fluctuation		0.04	0.04
Charge noise		0.38	0.38
Light noise		0.97	0.68

- The above value for the PDE assumes a reflection of at least 50 % due to the mismatch in refractive indexes between Si and LXe. A dedicated measurement of reflectance as a function of the angle of incidence on the SiPM surface is necessary and needs to be carried out in liquid xenon to reduce systematic uncertainties.
- The signal-to-noise ratio for single-photoelectron resolution is dependent on both SiPM gain and capacitance per unit area [24, 25]. This, under a power constraint, sets an upper limit in total area a channel can read out for a given sensitivity. The total instrumented photo-sensitive area will be $4\,\mathrm{m}^2$, and reaching a $10\,\mathrm{cm}^2$ detector unit with SiPMs is one of the goals of the nEXO Photo-sensor R&D.

The individual contributions to the overall energy resolution are summarized in table 3.1. Parameters such as dark noise and gain fluctuations of the SiPM are small enough that they do not increase the fluctuations substantially. The calculation for extracting individual components and their significance to the total resolution is partially based on [26].

Chapter 4

Characterization of Silicon Photomultipliers in the VUV

The focus of this chapter is on the performance study of VUV-sensitive SiPMs from the company Fondazione Bruno Kessler. It first starts with a technical overview of the vacuum SiPM test setup at Stanford University, that was used to characterize relatively large area SiPMs in the order of $\sim$ cm^2. The second part follows with a detailed description of the measurement procedure, including the calibration of the reference PMT, the estimate of the contribution from correlate noise and lastly the actual results on the PDE. Furthermore, the last part will discuss the importance of understanding the systematic errors and the reliability of the system.

4.1 Vacuum Test Setup for SiPMs

The vacuum SiPM setup at Stanford University was inherited from the EXO-200 experiment, for which an extensive characterization of the APDs was carried out [28]. With a couple of modification the setup is now used to study the performance of SiPMs in the VUV at 178 nm. The setup is optimized to accommodate relatively large SiPMs with a surface area of up to $2 \times 2\,\mathrm{cm}^2$. The vacuum chamber encloses the detector and source assembly, which can be seen in a sectional view in figure 4.1. Two level plates are mounted to a custom-made KF-60 flange with three rods holding the entire inner components in place. Polytetrafluoroethylene (PTFE) spacers in between the rods and the level plate guarantee an electric isolation from the rest of the system, which is crucial for low noise measurements. All feedthroughs are braced to the KF-60 flange at the bottom of the vacuum chamber.

The source assembly is a custom-made xenon scintillation light source with a platinum surface sealed inside a CF-flange in a xenon atmosphere at 1 bar. The platinum surface was electro-plated with ^{252}Cf by Eckert & Ziegler [29], which has a half-life of 2.65 yr and has two main decay modes. With a branching ratio of 96.9 % it decays under the emission of a α-particle with an energy of roughly 5 MeV and with a probability of 3.1 % it undergoes spontaneous fission. The energy release for spontaneous fission in the range of tens of MeV, gives a very bright and distinct signal from low light events such as from a α-decay or from dark noise and correlated avalanche events. A spectrum of the ^{252}Cf

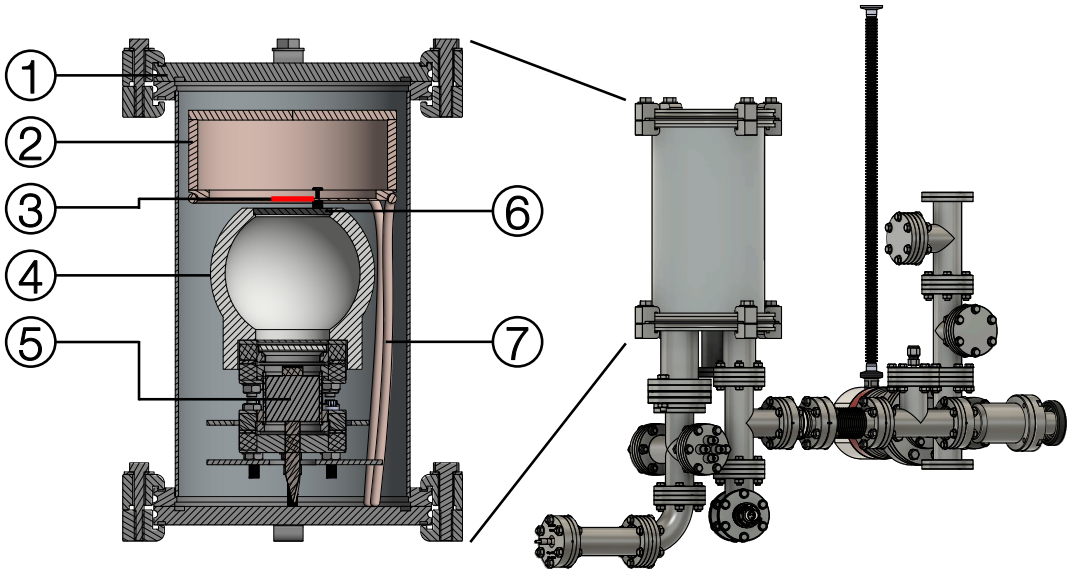

Figure 4.1: CAD model of the test setup at Stanford with a detailed view inside the vacuum chamber (1). A custom made flange (5) with a ^{252}Cf source, sealed inside a gaseous xenon atmosphere, is used as a scintillation light source with a wavelength at 178 nm. The detector cage (2) is a copper box with an inlet at the bottom (3) to fit the detectors. It is cooled through the copper box by a copper tube (7), that is braced onto it and flushed with liquid nitrogen boil-off gas. A PTFE sphere (4) is used to eliminate parasitic reflections off materials and in addition, a wavelength bandpass filter (6) is placed on top of the Teflon sphere to cut off light contaminations at larger wavelengths than 178 nm.

source is shown in figure 4.8 in section 4.3, where it will be discussed in more detail. In both cases one will get, due to the processes described in 3.2, xenon scintillation light at 178 nm.

The top flange of the source assembly has a quartz window through which the VUV light travels to the detector. The detector itself is placed at a distance of about 13 cm inside an inlet at the bottom side of the the copper box. This detector cage provides temperature uniformity due to the large heat capacity of copper. The copper box and, hence the detector, is cooled by flushing liquid nitrogen boil-off gas through a copper pipe that is braced to the lower perimeter of the copper box. The inlet accommodates detectors with a surface area of up to $2 \times 2\,\mathrm{cm}^2$. Due to the large solid angle of the quartz window the emitted scintillation light is likely to be reflected off materials, i.e. the rods or the stainless steel. This would lead to very large incident angles of up to 90° onto the detector surface. By simple Fresnel optics calculation one can see that there is a large dependence of transmittance from vacuum to Si on the angle of incidence and, hence on the PDE. Therefore, a sphere made out of PTFE, which is known to be a good reflector in the VUV range, with a cut-out on the bottom to fit on top of the source assembly and on the top to allow direct light to reach the detector. Photons that are emitted at very large angles will be reflected and confined within the sphere, until they eventually leave through the top cut-out under a small angle. This allows a clean measurement with less systematic uncertainties which is important for comparison of different devices. Furthermore, an optical band-pass filter from Pelham Research Optical [30], was placed in front of the detector to eliminate contributions from other wavelengths. The transmission spectrum of the filter has a maximum at 180 nm and has a width of 40 nm FWHM. Possible contamination could come from the re-transmissions of PTFE at higher wavelengths and the previously mentioned sub-dominant infra-red component of the xenon scintillation spectrum.

As an additional calibration light source, a multi-mode optical fiber with a core diameter of 600 µm from Thorlabs [31] was used. The benefits are varying light intensity and wavelength, ranging from 180 nm to 1150 nm. It was connected through a feedthrough to an aluminum box with a LED inside, that can be easily replaced. In order to be able to detect VUV light at all contaminations such as oxygen and hydrogen in the air have to be removed. The chamber can be maintained at a pressure of better than $1 \cdot 10^{-6}$ bar by using a two stage pump scheme with a dry scroll pump and a turbomolecular pump from Pfeiffer [32]. This goodness of vacuum is more than sufficient to make measurements at room temperature as well as at -104°C.

Lastly, the temperature of the copper box is measured with a 100 Ω Platinum Resistance Temperature Detection (RTD) sensor that is encapsulated in a copper block and threaded to the bottom side of the copper box close to the detector inlet. More RTDs were implemented to monitor the temperature of the xenon gas inside the source assembly, but not used on a regular basis yet. A possible temperature dependence of the scintillation yield would put additional systematic uncertainties on the measurements. Many precautions have been taken in order to electrically and thermally isolate the source assembly, i.e. by PTFE spacers. But over the course of several hours of data taking some temperature shift might still take place. The RTD signals are brought outside through a multi-pin feedthrough and readout by CNi3222 PID temperature control units from OMEGA [33]. These devices also drive two resistive heaters that regulate the temperature to $-104\,^{\circ}$C with an accuracy of 0.5 °C.

With all of the above, the setup was optimized to be able to quickly and reliably measure the PDE of SiPMs within 2 days.

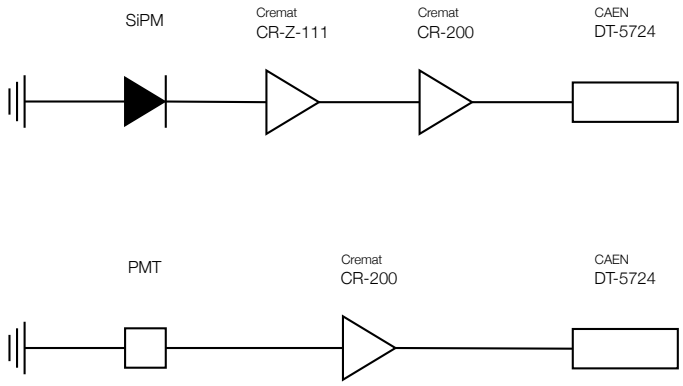

Figure 4.2: Readout chain for measurements with the SiPMs and the reference PMT. In both cases a high resolution waveform digitizer from CAEN was used for acquiring the data. Due to the intrinsically small output signal of a SiPM in the order of sub-mV, a preamplifier is used in addition to an Gaussian-shaping amplifier. On the other side, the PMT only needs the Gaussian-shaping amplifier. The shaping time of 1 µs is chosen to fit the digitizer's maximum sampling rate of 100 Ms/s.

4.2 Electronics and Data Analysis

The detector signal is transmitted via coaxial cables and through a grounded shield BNC feedthrough, which also transmits the SiPM bias voltage in the order of $30 - 35$ V. The reference PMT is operated at a voltage of 1190 V and uses a grounded shield SHV feedthrough. All the signal modification and data acquiring hardware is commercial. The SiPM signals are fed to a CR-Z-111 charge sensitive preamplifier from Cremat with a nominal gain of 0.13 V/pC. It consists of a FR-4 board with a voltage regulating component and a signal amplifying unit that can be used with different modules, provided by the company. For all measurements, that are presented here, the CR-111 module was used. The board is mounted inside a white painted aluminum box that serves the purpose of shielding the circuit from environmental pick-up noise. Due to the discharge of a feedback capacitor through a feedback resistor, the output signal is a long tailed pulse with a time constant of 150 µs. In the second step, the signal is further amplified and, more importantly, shaped by the CR-200 Gaussian-shaping amplifier from Cremat. Similar to the CR-Z-111, a CR-200 unit is placed inside a metal box. The shaping time was chosen to be 100 ns, which results in 240 ns wide (FWHM) Gaussian-shaped pulses.

The data is recorded and saved with a DT5724 digitizer from CAEN [34]. It has 2 channels, each with a 14 bit ADC and a sampling rate of 100 Ms/s. Waveforms were recorded for time windows between 5 µs and 10 µs and stored as binary files.

The analysis was done using a custom-made `C++`-software that utilizes the `ROOT`-package. It is a multi-stage analysis that first reads in a file, processes the data and saves all the waveforms in a `ROOT`-file. The next step is the extraction of key characteristics, such as the time stamps of the triggered pulse, the charge integral over 1 µs, the maximum value, the baseline value and the baseline fluctuation. The parameters are stored in a `ROOT`-file as well and allow a powerful multi-dimensional discrimination of bad data. The last step contains some more advanced fitting algorithms that, for instance, extract the

gain of the SiPM with a multi-Gaussian fit or the PMT's gain. These fit functions will be discussed in more detail in the dedicated sections within this chapter.

4.3 Absolute PDE Measurements

The measurements of absolute PDE concentrate on the new VUV-HD production of VUV-sensitive SiPMs from the company Fondazione Bruno Kessler (FBK) [35]. They were produced in two different sizes of approximately $6 \times 6\,\mathrm{mm}^2$ and $10 \times 10\,\mathrm{mm}^2$, each in a so-called low-field (LF) and standard-field (STD) version. Two of the wafers are shown in figure 4.3. The LF and STD versions differ in their doping profile and have significantly different behavior as will be seen in the following sections. The four wafers were received at Stanford University and were handled with high precaution using Latex gloves. They were already diced and attached to dicing tape and were easy to remove by using soft plastic tweezers.

An absolute measurement of efficiency, in contrast to a relative measurement, requires a calibrated reference detector. The latter one measures the efficiency ϵ_j of a SiPM for a particular wavelength λ_j relative to a known efficiency ϵ_i for a wavelength λ_i. However, photons of different wavelength behave differently at surface boundaries, making a reliable measurement, that could account for all systematic effects, very difficult. Therefore, given a stable light source, the comparison of the light yield of a detector with calibrated efficiency to a new device is less susceptible to errors from poorly estimated optical effects.

4.3.1 PMT Calibration

In order to reliably measure the absolute PDE of the SiPMs, a calibrated PMT (R9875P) from Hamamatsu was used as a reference detector. Given the known quantum efficiency (QE) and collection efficiency (CE) of the PMT and a proper calibration of the one

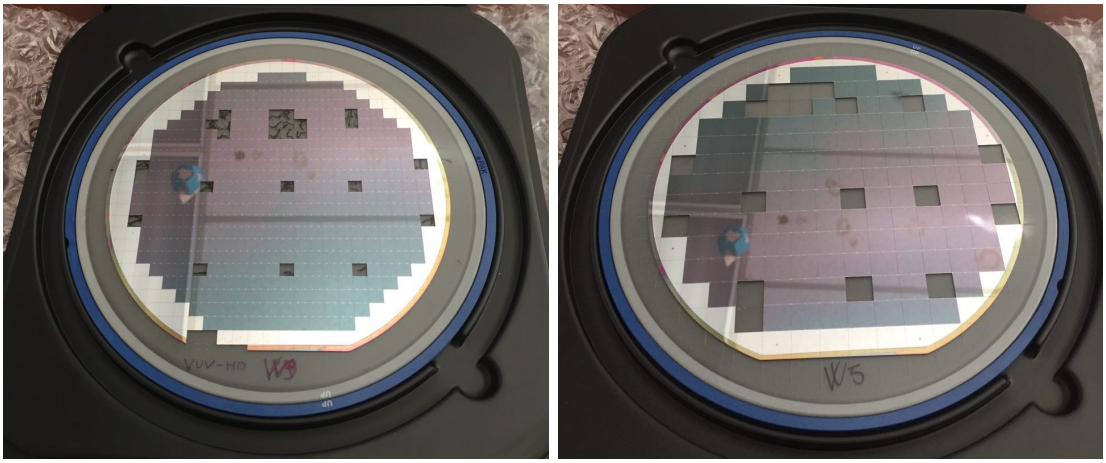

Figure 4.3: New production of VUV-sensitive SiPM from FBK. The left wafer contains the $6 \times 6\,\mathrm{mm}^2$ LF devices and the SiPMs in right wafer are the $10 \times 10\,\mathrm{mm}^2$ LF devices. The wafers were shipped as a whole, diced to separate individual SiPMs and attached to a dicing tape. These devices were handled with high precaution and removed from the wafer with soft plastic tweezers. The yield of SiPMs for the left and right wafer is 64 % and 50 %, respectively.

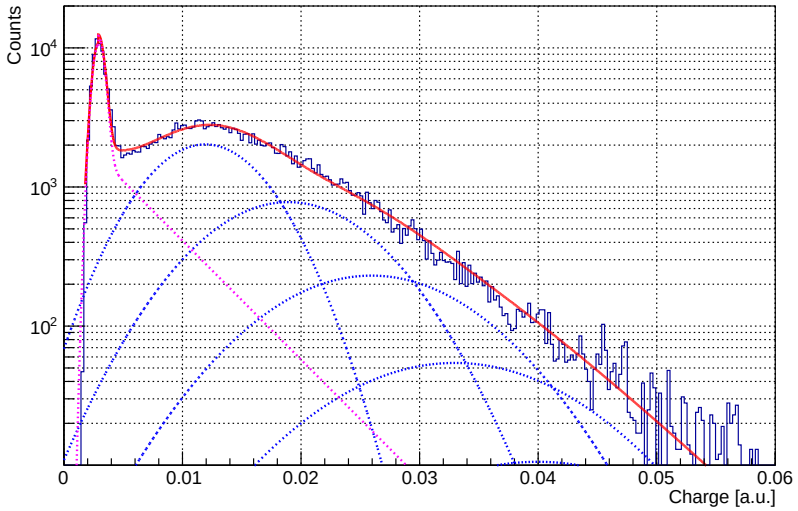

Figure 4.4: Typical response of the reference PMT at Stanford to a low light level LED. By fitting the function described in formula 4.4, the value for the 1 p.e. charge response Q_1 can be extracted and used to calibrate the PMT. The overall fit is shown in red, whereas the individual components of the fit are: background (pink), p.e. peaks(blue).

photon response, one can determine the amount of light detected by the reference detector. Together with the measured response of the SiPMs, one can translate this into an absolute PDE for the SiPM, which is described in more detail in 4.3.3. The single photon response is typically extracted from a measurement with a pulsed LED. The light level of the LED is set very low, such that the PMT detects only one photon once every ten LED pulses. The conversion of a photon into an electron follows a Poisson distribution where the probability to see n photons is

$$P(\mu, n) = \frac{\mu^n \mathrm{e}^{-\mu}}{n!} \tag{4.1}$$

where $\mu = m \cdot QE$ is the mean number of photoelectrons with m and QE being the mean number of photons that imping on the photocathode and QE the quantum efficiency, respectively. The subsequent process of amplification through the dynode system can be modeled as a Gaussian distribution and can be written for a more generic n photoelectron amplification case as

$$G_n(x) = \frac{1}{\sigma_1 \sqrt{2\pi n}} \exp\left(-\frac{(x - nQ_1)^2}{2n\sigma_1^2}\right) \tag{4.2}$$

assuming the amplification of the individual photoelectrons is independent. Q_1 is the average charge that is collected by the PMT for one photoelectron that is produced and σ_1 is the standard deviation of this charge distribution.

Together, the ideal PMT response S_{ideal} is a convolution of both processes and can be expressed as

$$S_{\mathrm{ideal}}(x) = P(\mu, n) \circledast G_n(x) = \sum_{n=0}^{\infty} \frac{\mu^n \mathrm{e}^{-\mu}}{n!} \frac{1}{\sigma_1 \sqrt{2\pi n}} \exp\left(-\frac{(x - nQ_1)^2}{2n\sigma_1^2}\right) . \tag{4.3}$$

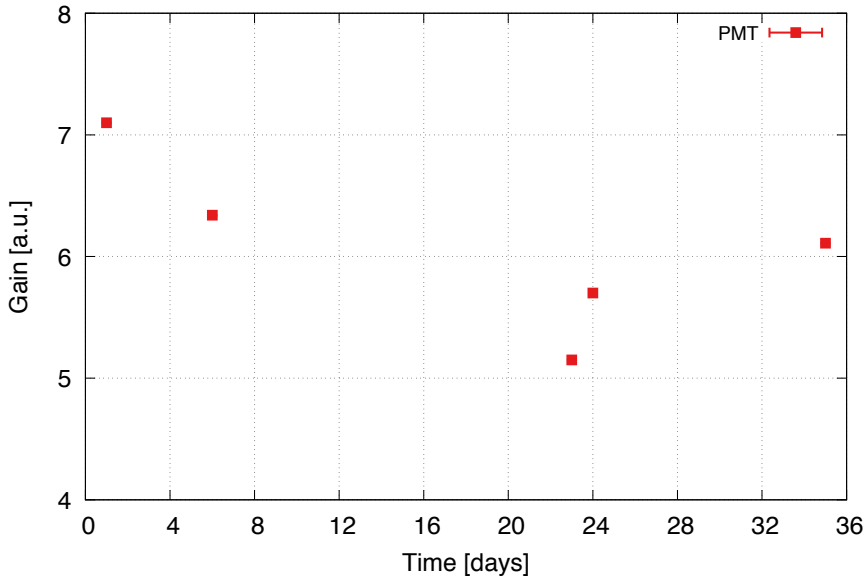

Figure 4.5: Fluctuation of PMT gain over the course of a few weeks.

However, one can think of various background processes that will contribute to the signal, e.g. thermoelectric emission from the photo-cathode or the dynodes, external or internal radioactivity or leakage current in the circuit that is connected to the anode of the PMT. Those lead to an additional charge noise contribution, that can be expected to decrease exponentially with charge [36]. Thus, the real PMT response will be another convolution of the pure signal response in 4.3 and the distribution of the noise contribution and can be expressed as

$$\begin{aligned} S_{\text{real}}(x) = &\left[\frac{1-\omega}{\sigma_0\sqrt{2\pi}} \cdot \exp\left(-\frac{(x-Q_0)^2}{2\sigma_0^2}\right) + \right. \\ &\left. + \ \omega \cdot \theta(x-Q_0) \cdot \alpha \exp\left(-\alpha(x-Q_0)\right)\right] \cdot e^{-\mu} + \\ &+ \sum_{n=1}^{\infty} \frac{\mu^n e^{-\mu}}{n!} \cdot \frac{1}{\sigma_1\sqrt{2\pi n}} \cdot \exp\left(-\frac{(x-Q_0-Q_{\text{sh}}-nQ_1)^2}{2n\sigma_1^2}\right) \end{aligned} \tag{4.4}$$

where ω is the probability for a background process to happen, α the coefficient of the exponential decrease of the discrete background process and μ the mean value of detected photons. Q_0, σ_0, Q_1 and σ_1 are the mean value and the standard deviation of the pedestal and the 1 p.e., respectively. Lastly, $Q_{\text{sh}} = \omega/\alpha$.

Over the course of a couple weeks the PMT calibration was repeatedly done to ensure the stability of the setup. Figure 4.5 shows the extracted gain values as a function of days from the first measurement. This variance has been accounted for by using the weighted mean to normalize the PMT charge spectrum and assign the error on this value as an additional systematical uncertainty. Section 4.4 will discuss possible explanation for this time variance.

4.3.2 SiPM Correlated Noise and Gain

To properly extract the information about the probability for a correlated avalanche to happen, the light source has to be blocked. Since the source assembly is a fixed part

of the setup and cannot be removed easily, a black rubber was placed on top of the wavelength band-pass filter, covering the whole surface area to absorb all the photons. The setup was pumped out and cooled down to $-104\,^{\circ}\mathrm{C}$ to minimize the contribution of dark noise, which is in the order of 1 Hz at these temperatures.

nEXO intends to integrate the collected charge over a time window of 1 µs, hence has no access to the composition of the additional charge contribution from correlated avalanches. The separation of these two effects requires a sophisticated fitting routine, that has the capability to distinguish pulses that are as close as a few ns [15]. The timing distribution then gives you, for a given model of AP and DN, their relative contribution within a given time window. CT is easier to access by only looking at prompt events, which is the pulse that the electronics has triggered on. The Stanford setup tries to mimic this readout scheme of nEXO by using long shaping times, as presented in section 4.2 and integrate the recorded waveform similarly over 1 µs. Even though the direct information about the individual components is lost, an analysis of the influence of the integration window on the overall correlate avalanche probability gives a rough idea about the composition. For instance, prompt optical crosstalk (CT) is happening effectively at the same time as the triggered pulse. On the other hand after-pulsing (AP) can have many different decay times depending on the lattice defect, possibly ranging from a few 10 ns to a few 100 ns. Assuming that AP is the dominant contribution to the overall correlated avalanche probability, the longer the integration time, the larger the contribution. Both processes depend on the over-voltage (OV) and typically increase with higher OV. AP eventually becomes so large, that it sustains the state of avalanche multiplication and increases exponentially. Also, for CT a quadratic increase with OV is observed.

For each waveform that is recorded, the integrated charge C_i is filled into a histogram. Depending on the purpose of the measurement, different metrics can be used to calculate a correlated noise probability P_{CN}. For this study two metrics will be presented and a motivation will be given for why only one of them is chosen later on. The first metric calculates the likelihood of causing a correlated avalanche. It does not include the order, i.e. a CT event followed by an AP event. In general, it can be expressed as

$$P_{\mathrm{CN}} = 1 - P_{1\,\mathrm{p.e.}} = 1 - \sum_{i=0}^{N_{\max}} N_i \qquad \text{for} \quad x_i < 1.5\,\mathrm{p.e.} \tag{4.5}$$

where N_i is the content of bin i and x_i the corresponding bin value in units of p.e and $P_{1\,\mathrm{p.e.}}$ is the probability for a 1 p.e. event to happen. It is a robust method of comparing the performance of devices across different vendors and their capability of handling or reducing correlated avalanches. However, given the concern described in section 3.3 about the additional contribution to the fluctuations in the light signal, this metric fails to deliver the correct estimate. It will tell you how likely it is that your fluctuations will be increased but not by how much. The second metric does include this information as it uses the mean number of additional avalanches per triggered avalanche and can be written as

$$P_{\mathrm{CN}} = \overline{N_{\mathrm{p.e.}}} - 1 = \frac{1}{\sum_{i=0}^{\infty} N_i} \cdot \sum_{i=0}^{\infty} N_i \cdot x_i \,. \tag{4.6}$$

The value that is obtained here will be used as a correction factor for the measured PDE. In order to properly apply this correction factor, the CN probability has to be calculated at every overvoltage (OV) at which a PDE measurement is done. The results for four

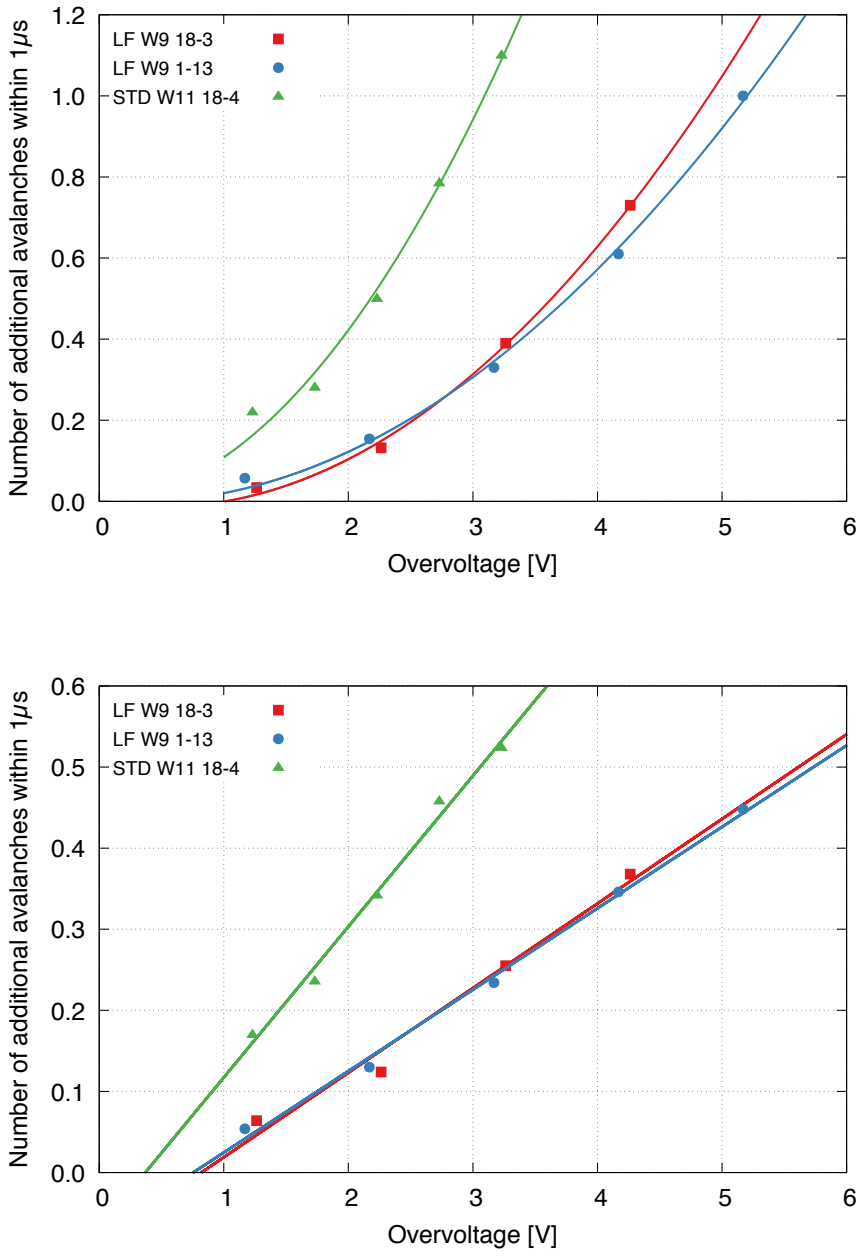

Figure 4.6: The contribution of correlated avalanches within 1 µs is shown as a function of OV. The top plot shows the metric that uses the mean number of avalanches and seems to agree reasonably well with the expectation to have a quadratic dependency on OV. The bottom plot shows the metric that uses the probability of triggering an additional avalanche independently of the contribution to the initial pulse, which suggests a linear dependency. In each case, the functions $f(x) = a \cdot x^2 + b \cdot x + c$ and $f(x) = a \cdot x + b$ were fitted to the data, respectively.

different devices for both metrics are shown in figure 4.6. The upper plot shows the mean number of additional correlated avalanches within 1 µs as a function of the OV. In addition, a quadratic function $f(x) = a \cdot x^2 + b \cdot x + c$ was fitted to the data to check the expected quadratic dependency on OV. This is due to the fact that CN depends on both, the total charge in the avalanche and the trigger probability, where either one also depends linearly on OV, hence CN $\propto$ OV^2. The metric in equation 4.5 is shown in the lower plot in figure 4.6.

In order to put the measurements of different devices in perspective, all results are typically shown as a function of OV. Therefore, the breakdown voltage has to be determined, to which the OV is referencing to. To do this, single Gaussian functions were fitted to the individual p.e. peaks in the charge spectrum to obtain the mean charge that corresponds to different amount of detected p.e. The top plot in figure 4.7 shows the mean charge as a function of number of p.e.'s of the LF W9 18-3 SiPM for different bias voltages. The slope of the linear function, that was fitted to the data, yields the gain of the SiPM for this particular bias voltage. Due to the good single photon resolution and the well-behaved operation of the SiPMs at smaller OV, the fit errors on the slope are on a sub-percent level, allowing an accurate gain calibration. This procedure has to be repeated for each bias voltage and for all devices to be able to extract the data, that is shown in the bottom plot in figure 4.7. The gain tells us the number of secondary electrons that are produced when triggering an avalanche. Per definition, the gain is 0 at the breakdown voltage and is expected to increase linearly with OV. Therefore, by plotting the gain as a function of the applied bias voltage and extrapolating the linear fit function to 0, the breakdown voltage can be determined reliably and accurately. From the plot one can deduce that the two LF devices behave similarly in terms of breakdown voltage. Furthermore, the two LF devices, that origin from the same wafer, indicate almost identical behavior with respect to gain.

4.3.3 Cf-252 Source Measurement and Results

Finally, to extract the PDE value the spectrum of the ^{252}Cf source has to be measured for both, the SiPM and the PMT. The same procedure as for the correlated noise measurement is applied with the exception that the absorbing rubber is removed to allow the scintillation light to reach the detectors. Figure 4.8 shows the spectrum of ^{252}Cf, that is measured by both detectors. In the case of the PMT, shown in green, a time trigger was applied to record all waveforms. This includes waveforms without any event. Those events are present in the very left relatively narrow Gaussian-shaped peak, also referred to as pedestal, where the width of the peak equals the electronics noise of the setup. Events with low light yield such α-particles can be seen in the bump right next to the pedestal, corresponding to few p.e. events. The distinct broad peak around 0.15 p.e./mm^2 are spontaneous fission events that produce a large amount of light. The width is due to the randomness and large variation in the amount of energy that the daughter nucleus receives after the decay. Nevertheless, the position of this peak yields the amount of light that is seen by the detector on average .

In the case of the SiPM, shown in blue, its good single photon resolution allows to estimate the light yield by counting the number of peaks. In the shown histogram one is able to resolve photons up to 21 p.e. With all the variables, that were described earlier in the previous sections, a PDE value can be extracted according to

$$PDE = \frac{\text{p.e.}_{\text{fission,SiPM}}}{\text{p.e.}_{\text{fission,PMT}}} = \frac{C_{\text{fission,SiPM}}}{CN_{\text{SiPM}} \cdot G_{\text{SiPM}} \cdot A_{\text{SiPM}}} \cdot \frac{A_{\text{PMT}} \cdot G_{\text{PMT}}}{C_{\text{fission,PMT}}}, \tag{4.7}$$

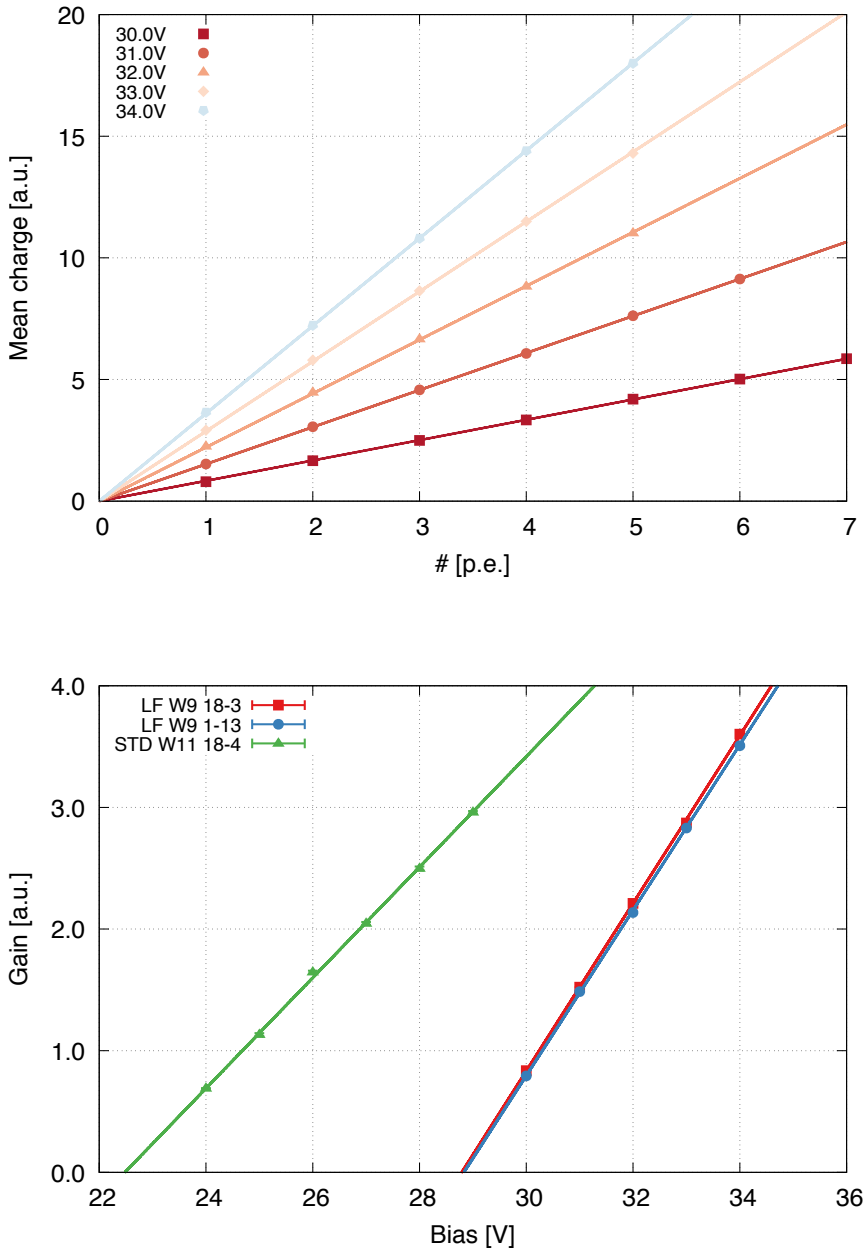

Figure 4.7: The two plots show the gain calibration and the breakdown determination for several devices. Exemplary for the LF W9 18-3 devices, the top plot shows the mean charge that is released for different number of p.e.'s. The slope of a linear fit function to the data yields the gain, that can be plotted as function of applied bias voltage, as shown in the bottom plot. Since per definition the SiPM does not have any gain below breakdown the zero of a linear fit function to the data corresponds to the breakdown voltage.

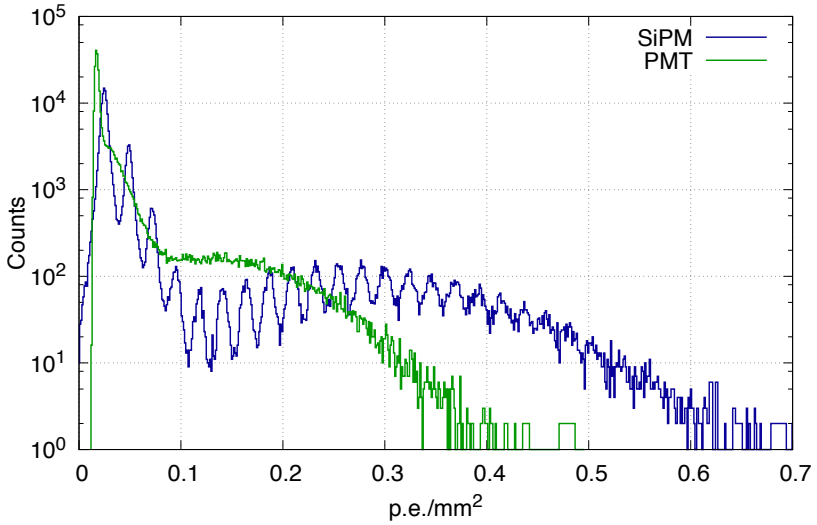

Figure 4.8: ^{252}Cf spectrum measured with a LF SiPM (blue) and the reference PMT (green). In the case of the PMT, one can divide the spectrum into three components starting from the left to right. The first peak is the pedestal, corresponding to the electronics noise of the setup, followed by a small bump that is due to α-particles. The broad peak around 0.15 p.e./mm^2 contains spontaneous fission events. The spectrum obtained with the SiPM, allows to resolve the single photon peaks, where the left part corresponds to dark noise events and α-particles and the broad distribution that is centered around 0.3 p.e./mm^2 is due to spontaneous fission events.

where A_i is the surface area, G_i the gain and $C_{\text{fission},i}$ the fission peak position in units of charge for both detectors, with $i \in \{\text{SiPM}, \text{PMT}\}$. The results are shown in three different ways in figure 4.9. The upper plots show how the PDE behaves as a function of the OV. The bottom plot shows the PDE as function of CN in units of additional avalanches within 1 µs, using the CN metric that uses the mean number of avalanches per parent avalanche.

Considering the bottom plot, due to reasons we pointed out earlier about the correct CN metric in 4.3.2, the LF devices seem to meet the requirements of nEXO in terms of PDE and CN. However, they exceed the minimal requirements barely. Moreover, it is not yet clear how stringent those limits are in order to reach the desired 1 % energy resolution. More generally, one can see that the LF devices perform better since they have significantly less CN for roughly the same PDE, which is consistent with the behavior in the plots in figure 4.6.

The error bars are statistical uncertainties from fitting variables such as SiPM and PMT gain and the fission peak position. The colored bands represent the systematical uncertainties, that are the same for all the measurements. Since each individual contribution to the total statistical error is on a sub-percent level, we rounded them all up to 1 % and assigned them to all the measurements similarly. The details about the sources of uncertainty and their values are described in more detail in the following.

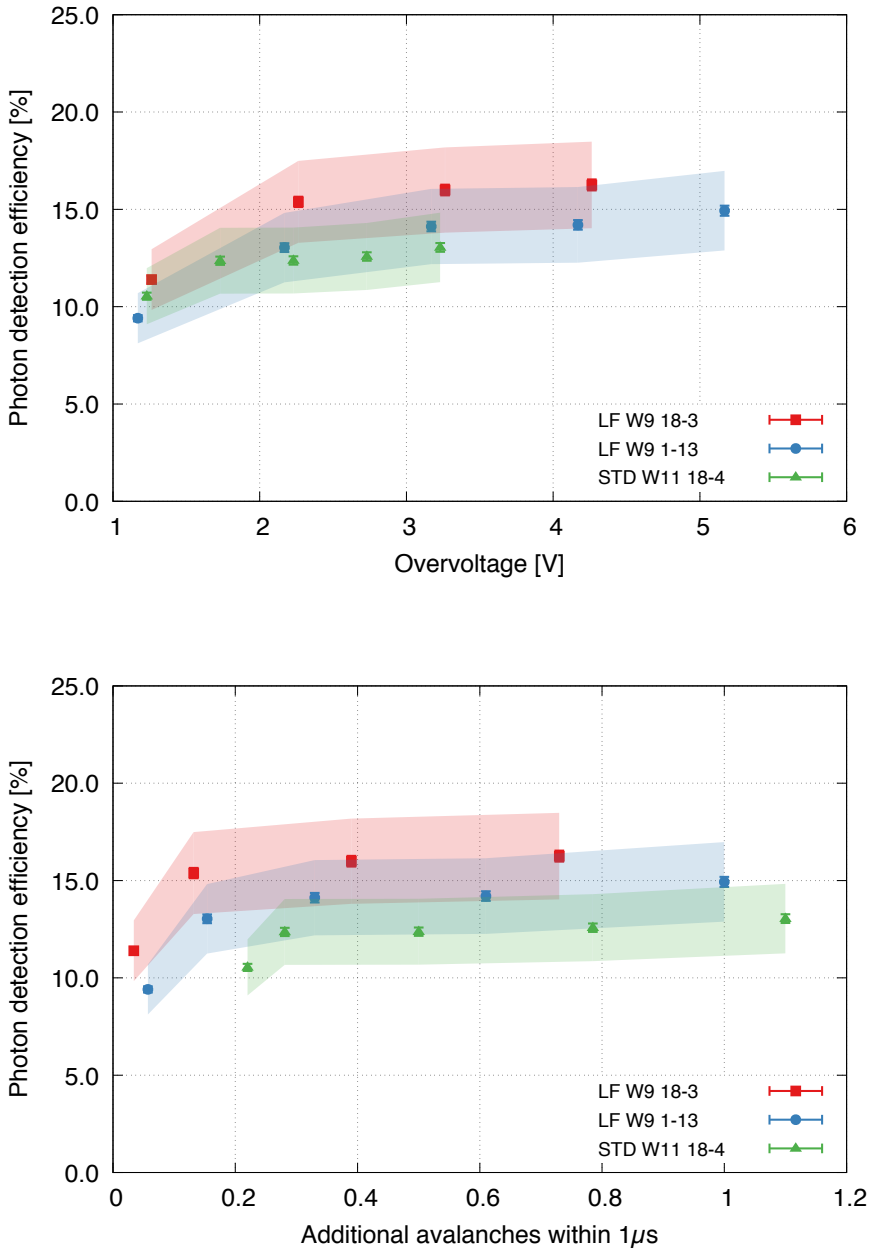

Figure 4.9: Results of the *PDE* measurements. The upper plot shows the increase of *PDE* with OV, whereas the bottom plot shows the more interesting case with *PDE* vs CN. The x-axis is in units of additional avalanches within 1 µs, which is equivalent to the anticipated integration window for nEXO. One can see that the LF devices meet, even though barely, the current requirements of nEXO.

4.4 Systematic Errors

The errors in all three plots in figure 4.9 origin from a careful analysis of potential sources for systematic and statistical uncertainties. The eight main component and their estimated values are summarized in table 4.1, where the major component, the PMT, is split into three sub-categories. Our reference PMT has been calibrated by Hamamatsu in order to get the respective wavelength-dependent QE and the CE of this particular tube. The QE was measured to be 14 % with an uncertainty of 2.1 %. For the CE a value of 70.6 % was determined by the company, however without an error. Conservatively, a 10 % error on this mean value was assumed. Furthermore, a variation of the PMT gain was observed and is shown in figure 4.5. There could be two reasons for that: 1) The mean Poisson rate was manually adjusted to 0.1 by counting the number of waveforms that passed before a PMT signal was seen. The fit model could, by unwillingly changing the mean Poisson rate μ in the fit function, yield slightly different values for the mean charge that is released for a 1 p.e. event. 2) The PMT itself is not stable over time, which could be either due to an unreliably working HV power supply or an internal time variance of the PMT. To account for the change in gain, the error on the weighted mean is included as an systematic uncertainty. The statistical uncertainty on the PMT gain itself is relatively small and well below 1 %, which is the value that was assigned. The bottom inlet of the copper box is designed such that all detectors are at the same height. In order to compensate a $1 - 2$ mm offset a 3 % systematic error is assigned. The value was concluded from an optical simulation of the setup with different detectors, using the Chroma software (see chapter 6). The SiPM gain calibration, as shown in section 4.3.2, can be performed very reliable and with an accuracy on a sub-percent level. This is also true for the position of the fission peak, which is extracted by fitting a Gaussian function. Both uncertainties were addressed with a 1 % error. However, in terms of the correlated noise correction, that was applied in the previous section 4.3.3, no accurate model is at hand to estimate the uncertainty for either one of the metrics in use.

Table 4.1: Summary of systematic and statistical error sources. The largest component of the uncertainty in measuring the PDE is the unknown CE uncertainty of the PMT. Since all error sources are independent, the components were added in quadrature which results in a total uncertainty of roughly 15 %.

Source of Error	**Value** [%]
Solid angle	3
PMT gain stability	8.6
PMT QE uncertainty	2.1
PMT CE uncertainty	10
Total	**13.7**
PMT gain calibration	1
SiPM gain calibration	1
Fission peak position	1
Total	**2**

Chapter 5

Towards a Liquid Xenon TPC with SiPM Light Readout

Prior of building nEXO, all the individual components need to be tested. The Stanford liquid xenon test setup was designed to carry out an extensive analysis and characterization of the proposed charge readout tiles for nEXO. The first part in this chapter gives a brief overview of the liquid xenon setup, but will only focus on the inside of the xenon cell. In the second section, some initial results on the charge readout tiles are presented. The main focus of this chapter is on the last part, which presents a prototype for a large area SiPM array for light detection in liquid xenon. It comprises the mechanical and electrical challenges and the anticipated integration into the system.

5.1 Liquid Xenon Setup

The TPC is made out of two 12" Conflat (CF) flanges connected to a 12" CF full nipple. All vacuum components in the system are commercial and made out of the 304 stainless steel alloy. The top flange has a few custom-made modifications, where 2-3/4" CF half nipple were braced onto, that allow to mount another 8 smaller 2-3/4" leak-tight flange assemblies. Each assembly is capable of storing 4 charge sensitive preamplifiers that are sealed inside a nitrogen atmosphere to prevent condensation on the electronics when being cooled down. The bottom flange is a reducer and has a quartz window attached to it. A PMT (9921QB) from Electron Tubes Limited is mounted against the quartz window from the outside and is used to detect the xenon scintillation light with a quantum efficiency of roughly $QE = 15\,\%$ at 178 nm.

The TPC itself contains a photo-etched stainless steel hexagonal mesh with a 95 % optical transparency and serves as the cathode with a nominal bias of 3110 V. It is mounted on the bottom flange and the distance between cathode and anode can be varied. Measurements so far were carried out at a drift length of either 18.2 mm or 33.2 mm with an average drift field of 936 V/cm. The anode is the charge readout tile, which is a $10 \times 10\,\mathrm{cm}^2$ fused quartz substrate and which was produced by collaborators at the Institute of Microelectronics (IME) of the Chinese Academy of the Sciences [37]. 30 strips in x-direction and 30 orthogonal strips in y-direction were deposited on the substrate,

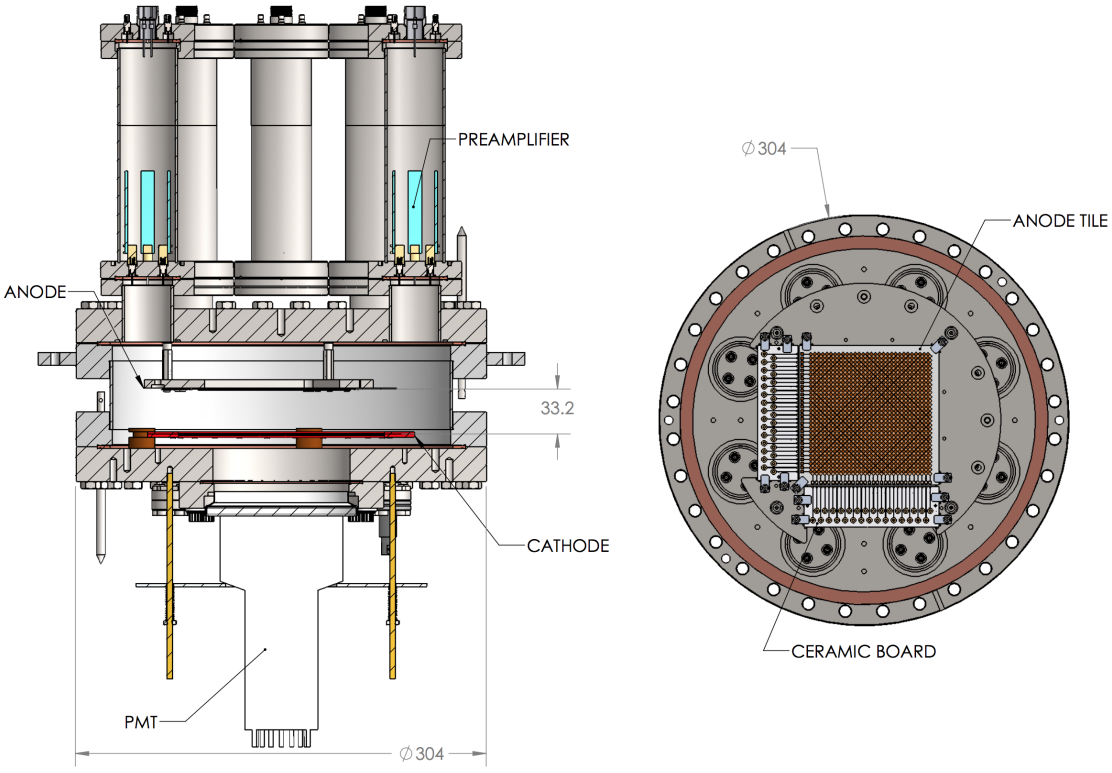

Figure 5.1: The TPC assembly that is used for characterizing the charge readout tiles for nEXO. It consists of two large 12" CF flanges with 304 mm in diameter and an inner CF full nipple. The top flange was modified to accommodate 8 smaller 2-3/4" (70 mm) CF flanges that store the charge sensitive preamplifier in a nitrogen atmosphere. A quartz window was attached to the bottom flange through which a PMT can detect the xenon scintillation light that is produced inside.

each of which is electrically isolated from the others. The strips are made up of 30 square pads that are connected at corners and have a length of 3 mm across the diagonal.

The entire setup is submerged in a large dewar filled with the HFE-7000 cooling fluid to ensure high temperature uniformity similar to EXO-200. The fluid, and therefore the cell, is cooled by flushing liquid nitrogen through a copper plate that surrounds the cell. The temperature is controlled by adjusting the liquid nitrogen flow rate. The system is set to operate at a pressure of about 1.2 bar and a temperature of 168 K, which is monitored by a thermocouple, attached to the copper plate. All environmental variables are readout by a LabView interface and are regulated through there as well.

5.2 Test of Charge Readout Tiles

Due to the lack of enough feedthrough and digitizer channels, the charge tile strips cannot be readout individually but need to be grouped. In total, 31 charge channels and 1 light channel are recorded. All 31 charge channels are further amplified by a custom charge-sensitive preamplifier, where the output experiences another tenfold amplification in a Phillips Scientific 776 amplifier before being digitized. The PMT signal is used as an event trigger and is therefore split in two. The first part is sent to an discriminator to generate a trigger and also veto the next 4.3 ms to limit the data rate to a value that is handleable by the hardware. The other part is amplified, shaped with a shaping time of 500 ns and then digitized. The digitizer is a 16-channel and 14-bit SIS3316 digitizer, which is set to a sampling rate of 25 MS/s. The recorded waveforms are 42 µs long. Given the drift field of 936 V/cm, the drift velocity of electrons is about 2 mm/µs, which results in a 16.6 µs delay between light and charge signal for a drift length of 33.2 mm. A sample event with a total charge energy of 1050 keV and all 32 data channels is shown in figure 5.3. This distinct feature allows to use the first few µs to be averaged over and subtracted

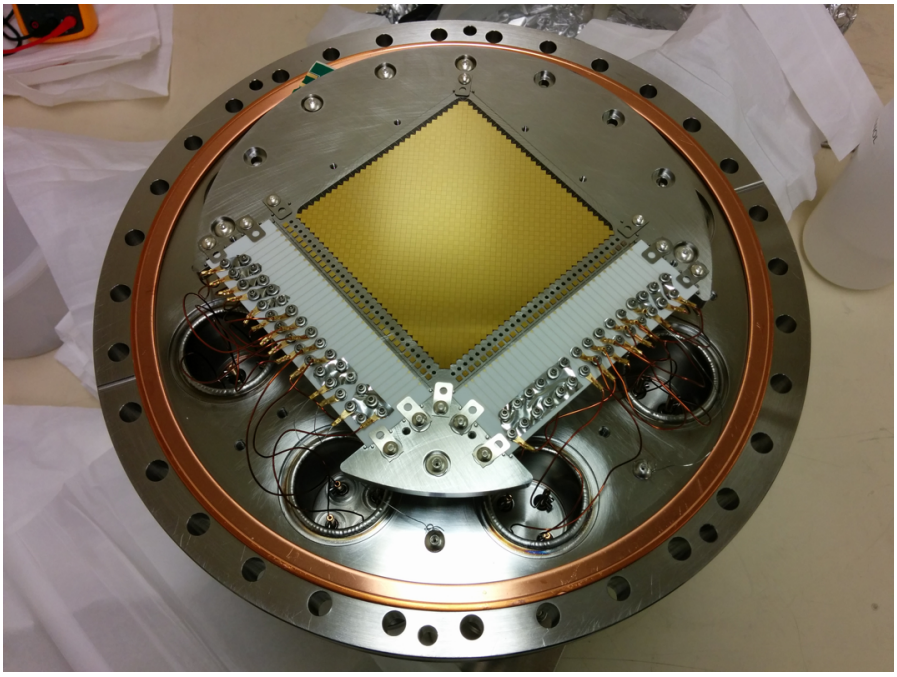

Figure 5.2: Prototype charge tile, that was produced by IME and is currently being tested in a liquid xenon setup at Stanford University.

from the waveforms as baseline. The sum of the last 11 µs gives the total energy in ADC units and needs further calibration to be translated into keV.

In order to have a realistic energy deposit similar to $0\nu\beta\beta$, a calibration source had to be found with close to MeV decay energy. ^{207}Bi proved to be the best candidate with an acceptable -half-life. A thin, 1.3 mm in diameter, wire made out of platinum-rhodium was plated with ^{207}Bi and curled around one of the meshes‘ hexagons. It predominantly undergoes electron capture with a half-life of 31.55 yr and releases a 1633 keV conversion electron in 87 % of the time. The excited ^{207}Pb daughter nucleus de-excites by emitting two consecutive γ-rays with an energy of 1064 keV and 569 keV [38], respectively. The latter one is the highest intensity peak in the ^{207}Bi spectrum and is used for energy calibration. This is done by using only events that hit a single channel to maximize the accuracy of the calibration. A fit function, consisting of a Gaussian and an exponential background, was fitted to the 569 keV peak, which is done on a channel-by-channel basis.

The current GEANT4 simulation of the setup also incorporates a full simulation of the drifting charge, that was adapted from previous EXO-200 Monte-Carlo simulations, an estimate of potential radio-active contamination, a detailed electric field map generated with COMSOL and a light collection map. The last item was built using the GPU-accelerated Monte-Carlo based ray-tracing software Chroma, that will be discussed in more detail in chapter 6. Altogether, it reaches a reasonable agreement with data and is able to reproduce the features in the spectrum. With the current charge tile an energy resolution of 5.6 % at the 569 keV peak was reached. In comparison, the expected intrinsic resolution of liquid xenon at 936 V/cm is 5.5 %.

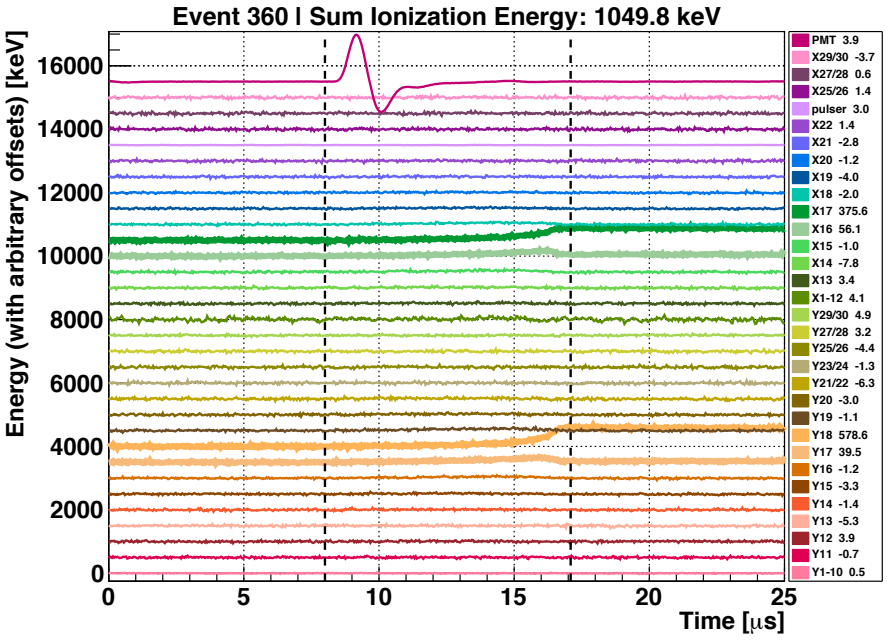

Figure 5.3: Recorded waveforms for all 32 channels for an examples event with a total energy of 1050 keV. The top waveform shows the PMT signal with a bipolar shape. The channels that were hit and collected charge are shown in bolt.

5.3 Silicon Photomultiplier Integration

The setup as described above does well in reconstructing the charge signal and achieve close to physically possible energy resolution for charge only. However, a validation for an improved energy resolution by combining the light and charge channel and make use of their anti-correlation has not been successful yet. This is mainly because of the following two reasons:

- The light collection efficiency of the PMT is not sufficient, yielding a large uncertainty in the light channel. There are three parts that contribute. (1) The distance between the photocathode and the TPC is $> 70\,\mathrm{cm}$ and results in a poor solid angle efficiency. (2) The already low amount of light that makes it to the quartz window is further attenuated by roughly $50\,\%$. (3) Even though the PMT was tightly pressed against the window, a remaining thin film of HFE-7000 between the PMT entrance window and the quartz window could be possible. However, none of the optical properties of this fluid for these wavelengths is known, making estimations on the attenuation difficult. Since it does contain oxygen, it seems likely to worsen the light collection efficiency. By placing a light detector in close proximity to the TPC and inside the LXe, all the above issues would be solved.

- The TPC does not cover the full volume of the xenon cell. Therefore, charge and scintillation light can be produced outside the active area, of which only the light will be detected by the PMT. The efficiency in the light channel is poor, which makes a reconstruction of those events difficult. Additionally, since those γ-rays are relatively high energetic, they are also likely to Compton scatter at least once. Hence, not all the energy of an event will be deposited inside the TPC, worsening the resolution.

These concerns lead to the motivation of integrating SiPMs into the system for more efficient light detection and to demonstrate the interplay of the novel charge and light readout that is planned for nEXO. To cover approximately the same photo-sensitive area

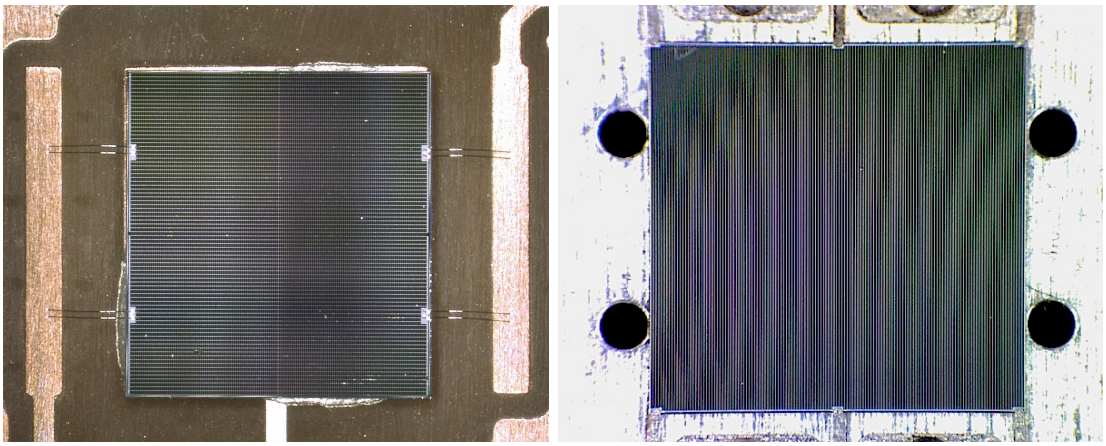

Figure 5.4: Magnified image of a small SiPM on the left side that was glued to a metallic pad and wire-bonded to the the top surface pads on the edge of the device. A set of two wire-bonds per pad was used for redundancy. The right side shows the new mounting method where the cantilever-based metallic clips hold the SiPM by pushing against the pads on the top surface.

as the PMT, that has a photocathode with 67 mm in diameter, 36 of the large LF devices from FBK need to be used. One condition for using such a high number of SiPMs for a prototype is the re-usability that also preserves the possibility of additional scrutiny by other setups. A possible mechanical and electrical mounting method will be presented in the following.

5.3.1 Cantilever-based Electrical Connection

The standard way to mount SiPMs is to use a conductive silver epoxy to glue the metal-plated backside of the SiPM on a gold pad on a carrier, which in the case of the FBK VUV-HD generation represents the connection to the anode. The cathode is either one of the wire-bonding pads on the edges of the top surface, where a wire-bond is connecting the pad to another gold pad on the same carrier. A microscope image of a mounted small LF SiPM is shown in figure 5.4. For reasons of chemical purity and outgassing, this method cannot be used in LXe which will be discussed in more detail in 5.3.2. Furthermore, these devices will not be removable anymore.

Inspired by the mounting scheme of the LAAPDs in EXO-200, a photo-etched and spring-loaded cantilever-based metallic clip was designed to not only hold the photo-detector in place but also makes electrical contact. The large LF SiPMs have six pads on the top surface that can be used for applying a load to hold them against a carrier, as can be seen on the right side in figure 5.4. The pads' dimensions of 0.28 mm × 0.10 mm make the task of mechanically connecting to the pads challenging.

The maximum deflection of a free hanging cantilever beam under the force of a concentrated load P at the end can be expressed as

$$\delta_{\max} = \frac{Pl^3}{3EI} \tag{5.1}$$

with the length of the beam l, the Young's modulus E and the moment of inertia $I = \frac{1}{12} \cdot w \cdot t^3$. The moment of inertia assumes a rectangular section with thickness of t and width w, where t is along the axis in which the bending deflection is applied. The

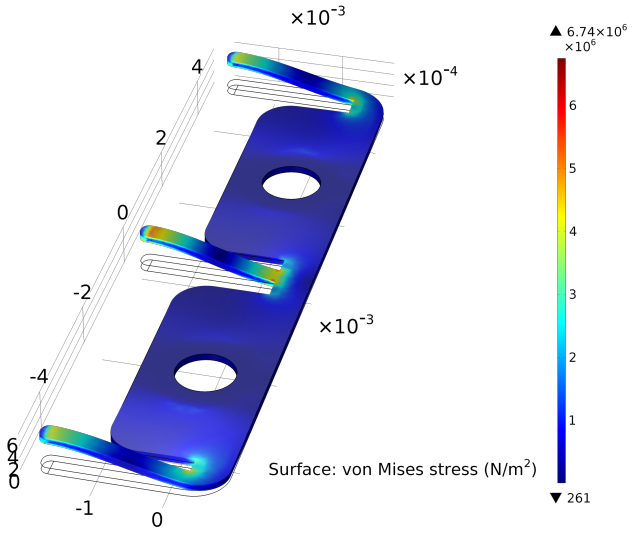

Figure 5.5: COMSOL simulation of the surface stress of the SiPM mounting clips due to the displacements of the cantilevers that push down on the on top of the SiPMs.

Table 5.1: Mechanical properties of the cantilever-based metallic mounting clips made out of stainless steel 304.

Property	**Value**
Young's modulus	200 GPa
Width	0.28 mm
Height	0.10 mm
Length	2.20 mm
Moment of inertia	$2.3 \cdot 10^{-5}\,\mathrm{mm}^4$
Tensile strength, yield	$2.15 \cdot 10^{8}\,\mathrm{N/m}^2$
Maximum stress	$6.74 \cdot 10^{6}\,\mathrm{N/m}^2$

maximum deflection $\delta_{\max} = 0.3\,\mathrm{mm}$ corresponds to the height of the SiPM. For the 304 stainless steel alloy a Young's modulus of $E = 200\,\mathrm{GPa}$ was used [39]. All parameters and properties for the prototype are summarized in table 5.1.

First, the required load to mechanically hold the SiPM in place, but also have sufficiently good electrical contact, needs to be determined. A measurement of the resistance between the metallic backside and a gold pad as a function of the load that was applied uniformly on the SiPM top surface was carried out. Applying a load of 30 g yielded a resistance smaller than 1 Ω and seemed sufficient. This results in a cantilever length of $l = 2.2\,\mathrm{mm}$.

In the second step, a CAD model of the mounting clip was created and fed into COMSOL to simulate the stress along the surface due to the deflection of the cantilever beams. The simulation shows a maximum stress of $6.7 \cdot 10^{6}\,\mathrm{N/m}^2$ along the interconnection of the cantilever beams and the main structure and close to the tips. This is still about 2 orders of magnitude smaller than the tensile strength of stainless steel 304 at which it starts to yield. The resulting surface stress is shown in figure 5.5.

Lastly, 700 mounting clips were photo-etched and gold plated for two reasons. In order to not damage the highly sensitive SiPMs, especially since a concentrated localized load is applied on the edges, a 2.5 µm gold layer makes the mounting clips softer and the surface less rough. In addition, gold has a better electrical conductivity which is desirable when dealing with fast and small signals.

The two bottom images in figure 5.6 show a first test assembly of 6 large LF devices on a plastic substrate with prototype mounting clips. Four white plastic dowels for each SiPM were used to confine their position on the surface. The three upper images in figure 5.6 were taken under a microscope and show a detailed view of the mounting clips and how they attach to the pads on top of the SiPM. The middle example shows a reasonably good alignment and connection, whereas the left one illustrates the difficulty in aligning on a sub-mm scale. The view on the right makes the roughness of the mounting clip surface and the potential danger of damaging the SiPM clear.

5.3.2 Vacuum and Liquid Xenon Compatibility

One of the main concerns for not installing a commercially available PMT in the xenon cell is potential contamination of the xenon, decreasing the life time of electrons significantly. The requirement of highest possible chemical purity puts a strong limitation on possible

materials that can be used for the integration of SiPMs. As a reference, the extensive list of vacuum compatible materials from the LIGO collaboration was used [40], even though our requirements are not a stringent as theirs. In terms of LXe compatibility, the knowledge from building EXO-200 served as guideline.

Generally, no component that contains any amount of plastic is used inside the xenon cell, because it is known to have a high outgassing rate and would contaminate the LXe. In terms of mounting, all parts such as screws, nuts and washers are made out of stainless steel 304. As SiPM carrier material a ceramic was chosen. Among a couple of possibilities, Al_2O_3 (Alumina) is the one that manufactures of printed circuit boards (PCBs) are standardly using. A ceramic PCB was designed to incorporate 6 SiPMs, which is shown as a CAD model at the top in figure 5.8. Six large gold pads are used to make electrical contact with the backside of the SiPMs. The mounting clips themselves are also screwed onto gold pads, using size 000 screws, washers and nuts from McMaster-Carr [41], which will be connected to the pads of the SiPMs. The signal of cathode and anode will be transfered to the backside of the ceramic carrier by through-ceramic-vias (TCV). Surface mount pins from Mill-Max [42] provide interconnectivity to signal cables via a push-on mechanism. The pins are made out of brass and plated with a 10 µm thick gold layer. Table 5.2 summarizes all the materials in use for the SiPM integration.

Prior to assembling, all component are subject to a cleaning procedure, which typically consists of a 20 min sonication in acetone and then ethanol. In between and after the two steps the parts are left to dry. Components that were modified in the machine shop were cleaned by an additional first sonication in simple green, a cleaner and degreaser that works well for removing oil residuals.

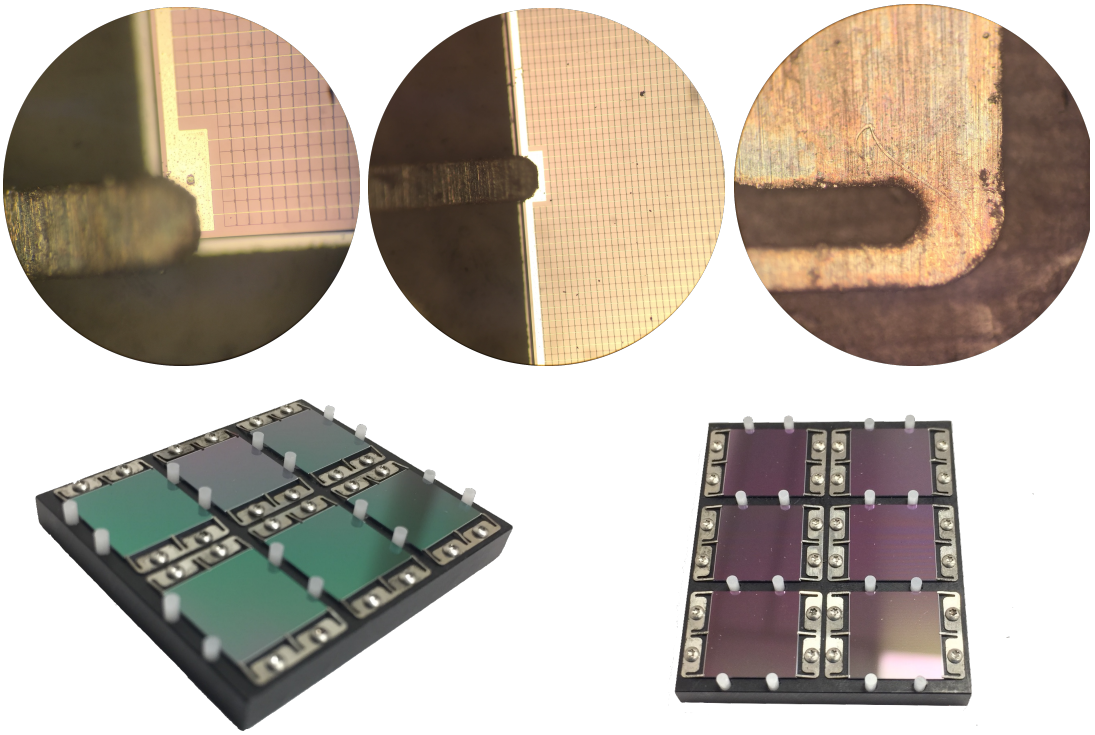

Figure 5.6: The bottom images show the first test assembly and proof of principle for this mounting method. The upper microscope images illustrate the difficulty with aligning the mounting clips on a sub-mm scale and with the rough surface finish.

Table 5.2: Composition of materials that were used for the SiPM large area assembly. Those materials were chosen based on the experience of the LIGO and EXO-200 collaborations on vacuum and liquid xenon compatibility.

Component	**Material**
SiPM	Si and SiO_2
Mounting clips	Stainless steel 304
Screws, nuts & washers	Stainless steel 304
Mounting carrier	Alumina ceramic (Al_2O_3)
Pads on carrier	Gold plated copper
Pins on carrier	Gold plated brass

Even though high precaution measures were taken to make the assembly as clean as possible, a last screening is done before eventually installing them in the LXe setup. The gas handling system features a residual gas analyzer (RGA) that is used to determine the composition of potential residuals. The measurement is based on mass spectroscopy. Before starting the scan the system needs to be pumped down to a pressure of below 10^{-8} bar. A RGA scan of a fully assembled ceramic board is shown in figure 5.7, indicating no presence of any suspicious residuals.

5.3.3 Large Area Assembly

The PMT that is currently used in the setup will be replaced together with the optical window flange. In order to maximize the light collection efficiency, the SiPMs need to be as close to the TPC as possible, but far enough to be not effected by the high and

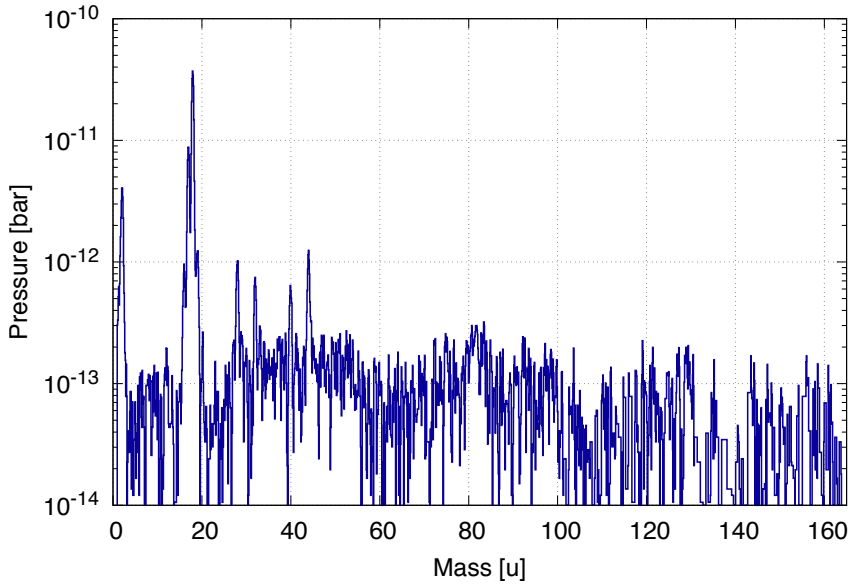

Figure 5.7: RGA scan of a fully assembled ceramic carrier, showing the density as a function of the atomic mass u. This spectrum indicates a clean environment without any potentially dangerous residuals in the vacuum system.

non-uniform electric field below the cathode. The bottom 12" flange of the cell in figure 5.1 is a reducer with an inner diameter of 101.6 mm and a thickness of 24.7 mm. The height of the array is chosen to be below the top edge of the flange to prevent a potential discharge to hit the SiPMs.

The next step to complete the integration into the LXe system is a holding structure for the ceramic carriers. A stainless steel support structure was designed with appropriate cutouts for easy interconnectivity of cables. It is mounted on a custom-made 6" Sub-D feedthrough flange with 100 pins, which is sufficient for connecting and reading out all SiPMs individually if needed. A 6" half nipple was welded to the feedthrough to serve as a containment for the preamplifier. The distance above the flange can be adjusted by different-sized spacers. The bottom of figure 5.8 shows a CAD model of the assembly.

On the other side of the feedthrough two boards are connected directly to the pins via a Sub-D connector. The boards were designed and fabricated by our collaborator at Oak Ridge National Lab, where each of them has 6 double-stage preamplifier channels. They were specifically made to allow the readout of up to 6 SiPMs connected in parallel. The limiting factor is the ratio of gain to capacitance per unit area of the SiPMs. In addition, the operational amplifiers that were used are known to behave properly and even better in terms of noise performance at cold temperatures. Therefore, the preamplification board will be kept in a nitrogen atmosphere that will be cooled down to liquid xenon temperatures together with the rest of the setup. The output of the preamplifier will be sent to the digitizer through 2 3/4" grounded-shield BNC feedthroughs.

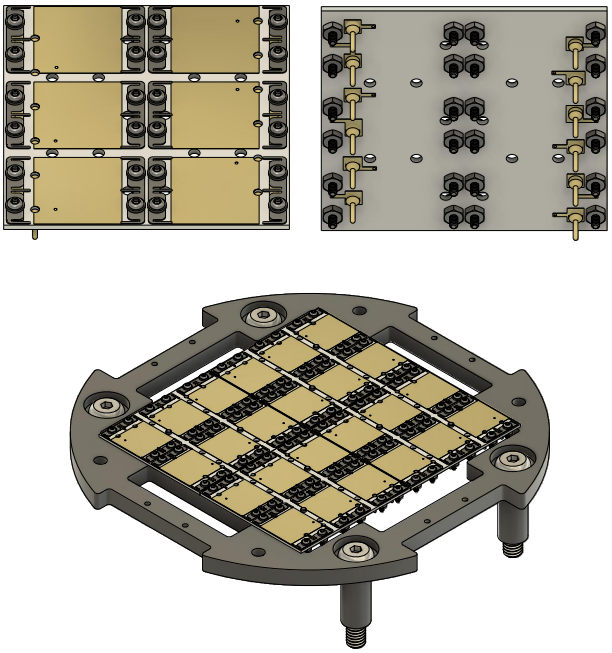

Figure 5.8: An orthographic view of the CAD model of the final design and the assembly of 4 ceramic carriers. A detailed description of the carrier can be found in the text.

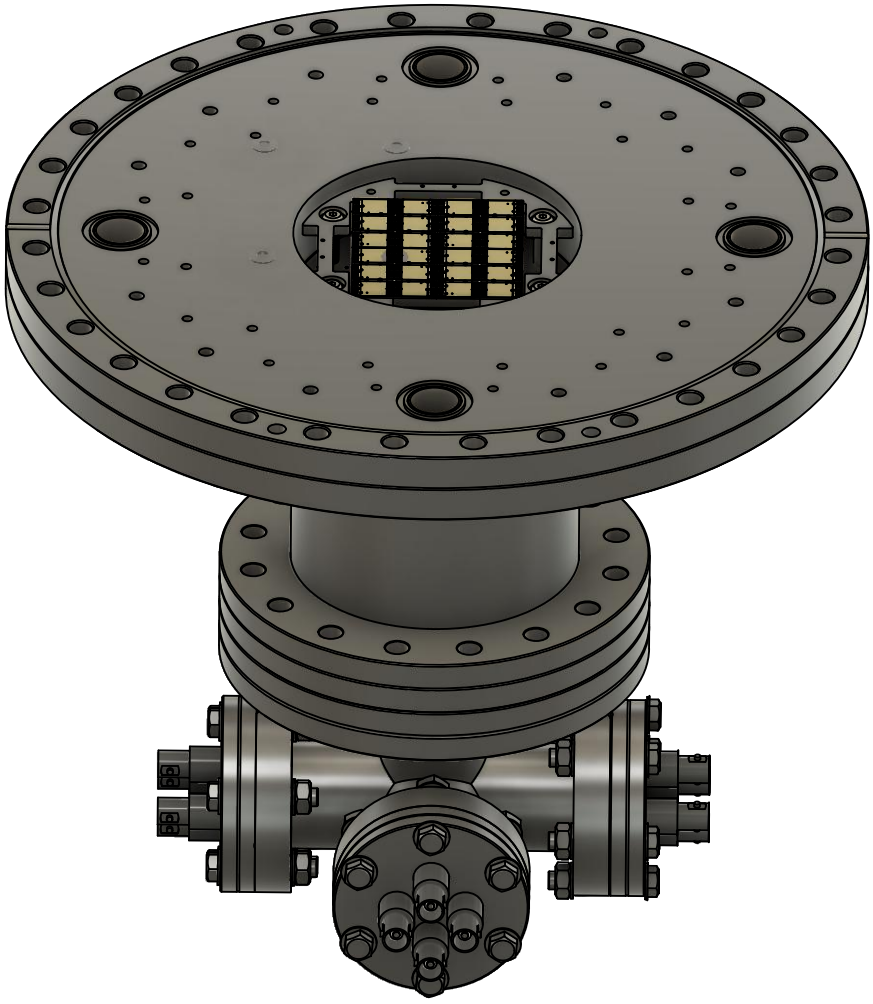

Figure 5.9: CAD model of the anticipated upgrade of the LXe test setup by including an array of currently 24, but ultimately 36, SiPMs for light readout. 4 ceramic carrier, with each having 6 $10 \times 10\,\mathrm{mm}^2$ SiPMs mounted onto it with the new cantilever-based mounting clips, are placed on a stainless steel holding structure. A Sub-D feedthrough with 100 pins provides enough channels to readout all SiPMs individually if needed. The inside of the nipple will be sealed in a nitrogen atmosphere and incorporates two custom-made preamplifier boards with each having the capability to readout up to 6 SiPMs at once when connected in parallel. The final output will be redirected to the digitizer outside the cryostat via grounded-shield BNC feedthroughs.

Chapter 6

Optical Simulations with Chroma

This chapter provides an overview of the simulation package Chroma, that was used for developing an optical simulation of the liquid xenon test setup at Stanford University. The basic functionality of the ray-tracing package, that Chroma uses, its advantages and disadvantages compared to the standardly used GEANT4 software will be summarized. The second part will concentrate on the implementation of the liquid xenon setup into the simulation, e.g. the detailedness and properties. This chapter will conclude with the generation of the light collection maps for the two different light readout detectors and present the results.

6.1 Overview of Ray-Tracing Package

Chroma is an open source software for performing Monte Carlo simulations of optical photons using surface-based geometries of detectors. It was developed by Stainley Seibert and Anthony LaTorre in 2011 as a different approach to the commonly used GEANT4 software [43]. It takes advantage of the development of CUDA by NVIDIA that allows general purpose computing, using graphics processing units (GPU), which can make Chroma up to 50 times faster than GEANT4. It is capable of simulating the physics of optical photons properly, which includes processes like:

- propagation through a bulk material
- refraction or reflection at boundaries due to indices of refraction
- absorption in a bulk material or at a surface
- Rayleigh- and Mie-Scattering
- diffuse and specular reflection at surfaces
- re-emission from wavelength-shifter.

In order to better understand the approach that is used by Chroma, a general and brief overview of the modeling in GEANT4 might be insightful.

6.1.1 GEANT4's Solid-based Modeling

In GEANT4, the "world" in which the simulation is done consists of several primitive solid volumes, like a sphere or a cuboid, that are usually described with only a few parameters. These simple primitive structures can be used to build more complex geometries, by applying boolean operations between two or more primitives, e.g. addition or intersection. This type of modeling is, opposed to the surface-based modeling described in section 6.1.2, an exact representation of the geometry. In addition, a tree-like structure is used to link different parts of the detector to each other. The highest structure in the tree hierarchy is the "world", in which everything takes places and which is the mother volume to all following daughter volumes. These daughter volumes themselves can again have other daughter volumes or sibling volumes, that are all not intersecting with each other. This tree structure is used to reduce the number of calculations for finding the next boundary intersection. However, with many sibling volumes and complex geometries this tree approach comes to a limit.

6.1.2 Chroma's Surface-based Modeling

Chroma uses flat triangles, as it is the most primitive two-dimensional structure, which is repeated many times to cover the surface of an object and that is usually called a triangle mesh. Each triangle vertex has a number assigned, which sets by applying the right-hand rule the normal of the surface, as shown in figure 6.1. This way an outside and an inside material can be specified for each individual triangle, making it more flexible in defining complex surface properties, e.g. different reflectivity of adjacent regions of the same object. For a proper simulation, internal consistency requirements of this modeling have to be followed, forcing non-closed surfaces to have the same material for inside and outside. This is shown in figure 6.2, using a schematic model of the nEXO copper vessel with some fictive non-closed surface extensions of the vessel. There is a trade-off in using

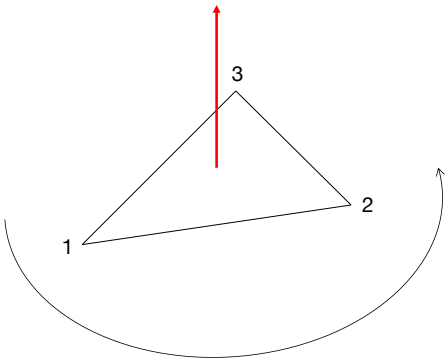

Figure 6.1: Definition of the normal vector by numbering the vertices in an oriented triangle. The red arrow show in the direction of the normal vector to the surface and indicates the outside material. The opposite side is therefore the inside material.

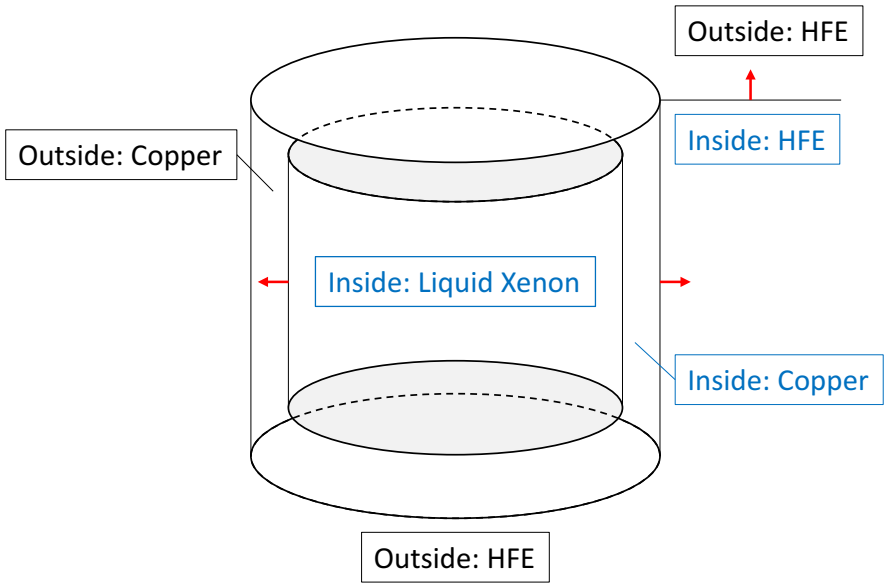

Figure 6.2: Internal consistency requirement for a schematic detector construction of the nEXO copper vessel. Non-closed surfaces have to have the same material for the outside as well as for the inside. The red arrows show in the direction of the normal vector to the surface and point towards the outside material.

flat triangles for building a geometry since it can only be an approximation due to the finite number of triangles that are used to mesh the surface. This could be overcome by using a more complex primitive, for example curved Beziér triangles, which would come at the expense of more complex coding for the implementation and more memory usage.

After defining the geometry, the world consists of a single list of all the triangles, which would make the calculation of the next boundary intersection of photons very slow. Similarly to GEANT4, some kind of tree data structure is used, where in the case of Chroma a *Bounding Volume Hierarchy* (BHV) is realized. The BHV consists of several axis-aligned boxed that work as bounding volumes and can include daughter bounding volumes. In contrast to GEANT4, sibling volumes are allowed to intersect and the primitive triangles can be inherited by several bounding volumes. An intersection of

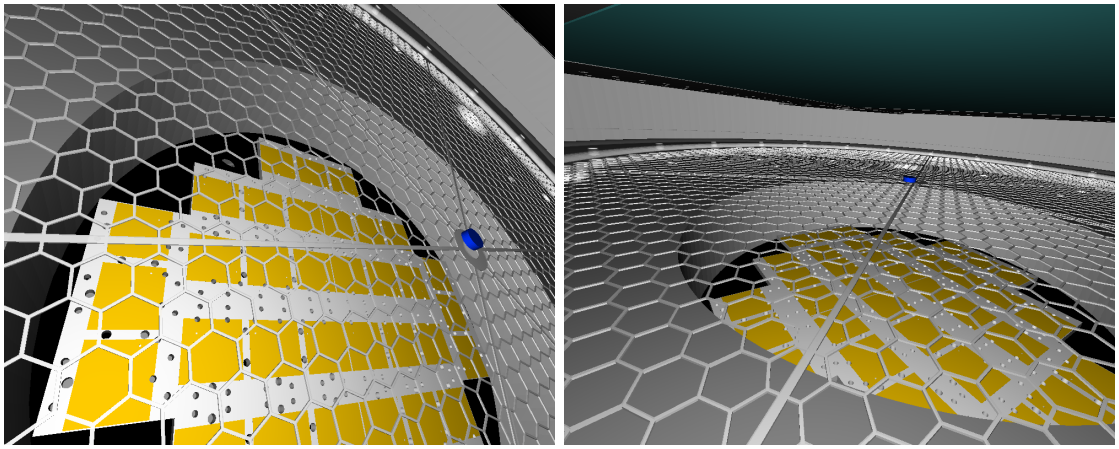

Figure 6.3: Example of the built-in rendering capabilities of Chroma. Very fine and complex geometries, such as the depicted cathode mesh and SiPM array underneath can easily be imported from a STL file and can be used in the simulation. The blue cylinder represents the position of the ^{207}Bi source.

a particle is tested by starting from the root of the tree and searching for the associated box until the leaf node is found.

A huge advantage of the surface-based modeling using triangle meshes is the feature to import geometries from typical computer-aided design (CAD) software as STL files. A typical rendering of an imported geometry is shown in figure 6.3. More details about the software can be found in [43].

6.2 Simulation of Liquid Xenon Setup at Stanford

Because of its speed performance, Chroma was used for developing an optical simulation of the Stanford liquid xenon setup, that was described in chapter 5. The main purpose was to generate a light collection map, that for each point in space inside the cell yields the probability for a photon to reach the photo-sensor and be detected. Typically, solid angle and detection efficiency considerations are sufficient to estimate the light collection efficiency to 0^{th} order. However, in general this very rough approximation holds only true for normal incidence and, more importantly, it does not account for reflections off

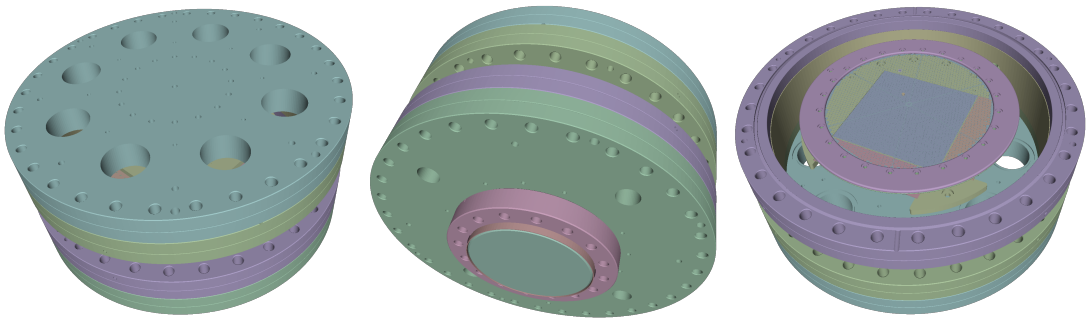

Figure 6.4: Different views of the model, that was used for the Chroma simulation. It only includes parts, that are considered to be potentially hit by photons. However, this does not yet include any photo-detector, i.e. the PMT or the SiPM array.

surfaces inside the cell. Using Chroma, many problems, that are analytically either not at all or only approximately solvable can be simulated.

Prior to importing the CAD model of the liquid xenon setup, a selection of necessary individual components out of the more than 1500 components was made. Only parts that might eventually be hit by a photon were considered, which reduced the number of final objects to 16. Also, many smaller objects such as bolts, nuts, clips, rods and other mounting parts have not been included in order to not slow down the simulation. The final selection of the detector is shown in figure 6.4. Most of the material inside the detector consists of stainless steel, where the 304 alloy was used consistently throughout the system. In order to make the light simulation as accurate as possible, many optical parameters of all the materials that were used need to be known. Unfortunately, many values for optical parameters of materials in the VUV are not known precisely. Therefore, some assumptions or simplifications had to be made, i.e. making all the stainless steel CF flange components in the system fully absorbing.

6.3 Light Collection Map

The creation of a light collection map requires emitting photons throughout the cell. For each point within the cell, the light map yields the response of the light readout detectors as the ratio of the detected light to the emitted light. This is also referred to as light collection efficiency (LCE). To increase the accuracy of the LCE, the simulation is repeated 100 times for each point, where the number of photons per run needs to be large enough in order to be able to detect a decent amount of photons. The mean value of the LCE distribution of each location over the multiple runs is used to create the light collection maps in figure 6.5.

Due to the approximate cylindrical symmetry of the setup, only a slice through the cell in z-direction and in radius is simulated and shown. To match the meshing of the electric field simulation, a step size of 2 mm in both directions is chosen. This is crucial since the amount of scintillation light that is produced is dependent on the electric field strength. The coordinate system center at $r = 0$ and $z = 0$ is located at the center of the charge readout tiles. The $z-$axis points towards the cathode mesh and, therefore all the data points below $z = 1.8\,\text{mm}$ correspond to locations within the TPC drift region. The point at $z = 1.8\,\text{mm}$ and $r = 0.2\,\text{mm}$ in both light collection maps in figure 6.5 with the suspiciously low efficiency is due to the center ring of the cathode mesh, in which the photons are produced.

The bottom plot in figure 6.5 shows the light collection map for the PMT. Due to several effects, only a poor LCE of $0.2 - 0.3\,\%$ inside the TPC below $z = 1.8\,\text{mm}$ can be achieved. The main reasons are a small solid angle and the additional attenuation in the quartz window. This inevitably results in a low photon detection rate and, consequently a large statistical error on the light channel. Therefore, it was not yet possible to make a successful energy measurement with the PMT.

However, the SiPMs' light collection efficiency, shown in the top plot in figure 6.5, shows an increase inside the TPC drift region to up to 2.5 %. With the almost tenfold improvement, an energy measurement using the light channel should be possible. Assuming that a 1 MeV electron will produce roughly 22 000 photons at an electric field of 1 kV/cm, on average about 550 photons will be detected by the SiPMs on average. This yields a relative uncertainty in the light channel of roughly 4 %, assuming Poissonian errors. In comparison, the PMT would detect on average about 66 photons with a relative uncertainty of 12 %.

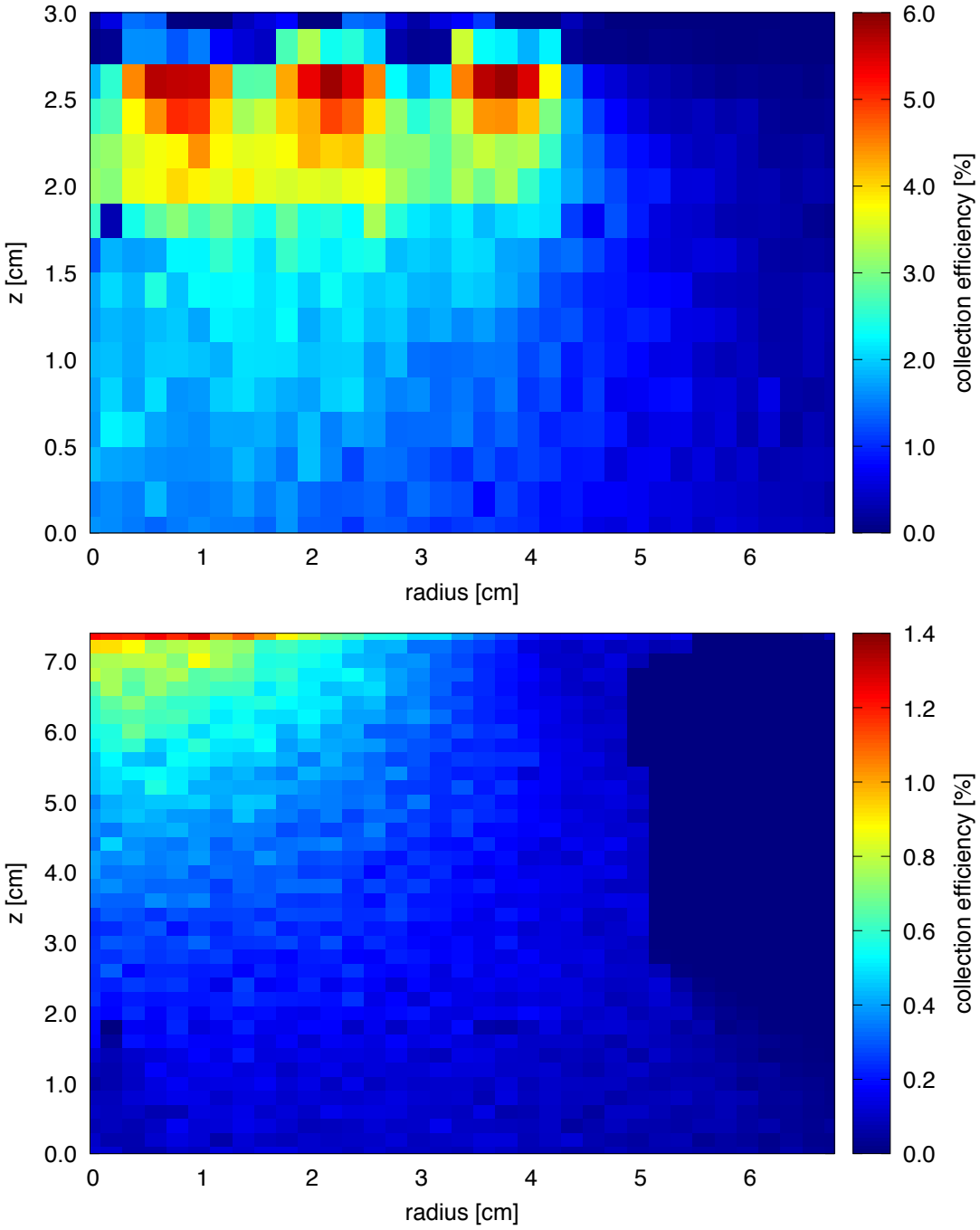

Figure 6.5: Light collection map for events inside the xenon cell, using the PMT (bottom) and the SiPM array (top). The point $z = 0$ and $r = 0$ corresponds to the center of the charge readout tile. Positive z-direction points towards the cathode mesh, which is at a distance of about 1.8 cm. The light collection efficiency for light coming from within the TPC rises from values around $0.2 - 0.3\,\%$ to $1.5 - 2.5\,\%$ when using the SiPM array instead of the PMT.

Chapter 7

Summary and Outlook

This thesis presented research on light detection for the future tonne-scale double-beta decay experiment nEXO. Silicon Photomultipliers have been studied as a novel and potential candidate for replacing commonly used APDs or PMTs. This included the characterization of different new devices from FBK, the development of a large area integration of SiPMs into liquid xenon and a proper optical simulation to generate a light collection map of the test setup at Stanford University.

The performance studies of the VUV-HD generation from FBK were carried out in a vacuum setup, that has been improved in terms of systematical uncertainties. Its design was optimized for a fast and accurate measurement of absolute PDE values for the 178 nm scintillation light. The calibrated PMT added the largest contribution to the overall uncertainty. Nevertheless, a sophisticated photon response model for the PMT was introduced and tested, that helped to reliably extract the gain of the PMT. The distinct position of the fission peak in the ^{252}Cf energy spectrum served as a calibration reference. A comparison of the fitted fission peak positions, which equals the mean number of detected photons, for the reference PMT and the SiPM, gives the relative light yield seen by the SiPM. This can then be translated into a PDE value. Currently, we set the PDE to be at least 15 %. At the same time the contribution from CN per parent avalanche should not exceed 20 %. The results indicate that the new VUV-HD SiPMs meet the nEXO requirements in terms of PDE and CN and could be a potential candidate.

After finding a suitable candidate, the integration of a large area SiPM assembly into the liquid xenon test setup at Stanford was planned. For this purpose, a cantilever-based mounting clip was designed that allows an easy assembly of up to 36 SiPMs. The design was inspired by the mounting method of the EXO-200 APDs. High precautions were taken in order to make all components highly vacuum and LXe compatible. A prototype has verified the proof of principle for such a mounting scheme, what ensure reusability of the SiPMs afterwards. Therefore, some final testing is undertaken before eventually installing the SiPMs into the LXe test setup. This would be the first system to use both, the new charge and light readout detectors for nEXO, to make measurements and take advantage of the intrinsic anti-correlation of the charge and the scintillation light.

An optical simulation with the Monte-Carlo-based Chroma software was developed to quantify the improvement in light collection by installing the SiPMs in to the LXe setup and replacing the formerly used PMT. Unlike GEANT4's volume-based geometry, Chroma uses surface-based geometries, which together with its GPU-acceleration and its data structure allows a much faster ray-tracing. The generated light collection map, which yields the detection probability of photons from any given point within the cell, shows an almost tenfold improvement within the TPC drift field. This lowers the statistical fluctuation in the light channel and makes an energy measurement with the combined light and charge energy possible.

Going forward with the nEXO R&D, the systematical uncertainties of the PDE measurement, dominated by the reference PMT, have to be further reduced in the vacuum setup and the obtained values need to be cross-checked. Furthermore, one still needs to work closely with the SiPM vendors to optimize critical properties, such as reducing correlated noise or increasing the PDE. The cantilever-based mounting clip is a first step towards a large area mounting concept, that needs to be further investigated and optimized in order to be a liable option for nEXO. Lastly, Chroma has proven to be a useful package for light simulations and is of huge interest when trying to optimize the optical properties of the nEXO TPC due to Chroma speed performance. This could help pushing the energy resolution even further below the 1 % goal.

Appendix A

List of Figures

Appendix B

List of Tables

Appendix C

Bibliography

[1] F. Englert and R. Brout. "Broken Symmetry and the Mass of Gauge Vector Mesons". In: *Phys. Rev. Lett.* 13 (9 1964), pp. 321–323. DOI: 10.1103/PhysRevLett.13.321.

[2] P. W. Higgs. "Broken Symmetries and the Masses of Gauge Bosons". In: *Phys. Rev. Lett.* 13 (16 1964), pp. 508–509. DOI: 10.1103/PhysRevLett.13.508.

[3] G. Aad et al. "Observation of a new particle in the search for the Standard Model Higgs boson with the ATLAS detector at the LHC". In: *Phys. Lett.* B716 (2012), pp. 1–29. DOI: 10.1016/j.physletb.2012.08.020.

[4] S. Chatrchyan et al. "Observation of a new boson at a mass of 125 GeV with the CMS experiment at the LHC". In: *Phys. Lett.* B716 (2012), pp. 30–61. DOI: 10.1016/j.physletb.2012.08.021.

[5] Q. R. Ahmad et al. "Direct evidence for neutrino flavor transformation from neutral current interactions in the Sudbury Neutrino Observatory". In: *Phys. Rev. Lett.* 89 (2002), p. 011301. DOI: 10.1103/PhysRevLett.89.011301.

[6] B. T. Cleveland et al. "Measurement of the Solar Electron Neutrino Flux with the Homestake Chlorine Detector". In: *The Astrophysical Journal* 496.1 (1998), p. 505.

[7] M. Altmann et al. "Complete results for five years of GNO solar neutrino observations". In: *Phys. Lett.* B616 (2005), pp. 174–190. DOI: 10.1016/j.physletb.2005.04.068.

[8] T. Araki et al. "Measurement of Neutrino Oscillation with KamLAND: Evidence of Spectral Distortion". In: *Phys. Rev. Lett.* 94 (8 2005), p. 081801. DOI: 10.1103/PhysRevLett.94.081801.

[9] Z. Maki, M. Nakagawa, and S. Sakata. "Remarks on the Unified Model of Elementary Particles". In: *Progress of Theoretical Physics* 28.5 (1962), p. 870. DOI: 10.1143/PTP.28.870.

[10] N. Arkani-Hamed et al. "Phenomenology of Electroweak Symmetry Breaking from Theory Space". In: *Journal of High Energy Physics* 2002.08 (2002), p. 020.

[11] E. Majorana. "Teoria simmetrica dell'elettrone e del positrone". In: *Il Nuovo Cimento* 14.4 (1937), p. 171. DOI: 10.1007/BF02961314.

[12] I. Ostrovskiy and K. O'Sullivan. "Search for neutrinoless double beta decay". In: *Mod. Phys. Lett.* A31.18 (2016). [Erratum: Mod. Phys. Lett.A31,no.23,1692004(2016)], p. 1630017. DOI: 10.1142/S0217732316920048,10.1142/S0217732316300172.

[13] F. Maltoni, J. M. Niczyporuk, and S. Willenbrock. "Upper Bound on the Scale of Majorana-Neutrino Mass Generation". In: *Phys. Rev. Lett.* 86 (2 2001), pp. 212–215. DOI: 10.1103/PhysRevLett.86.212.

[14] J. J. Gomez-Cadenas et al. "The Search for neutrinoless double beta decay". In: *Riv. Nuovo Cim.* 35 (2012), pp. 29–98. DOI: 10.1393/ncr/i2012-10074-9.

[15] I. Ostrovskiy et al. "Characterization of Silicon Photomultipliers for nEXO". In: *IEEE Transactions on Nuclear Science* 62.4 (2015), pp. 1825–1836. DOI: 10.1109/TNS.2015.2453932.

[16] J. Schechter and J. W. F. Valle. "Neutrinoless double-β decay in SU(2)×U(1) theories". In: *Phys. Rev. D* 25 (11 1982), pp. 2951–2954. DOI: 10.1103/PhysRevD.25.2951.

[17] S. M. Bilenky and C. Giunti. "Neutrinoless Double-Beta Decay: a Probe of Physics Beyond the Standard Model". In: *Int. J. Mod. Phys.* A30.04n05 (2015), p. 1530001. DOI: 10.1142/S0217751X1530001X.

[18] *Aurubis*. https://www.aurubis.com/en. Accessed: 2017-06-05.

[19] *3M*. http://www.3m.com/. Accessed: 2017-06-06.

[20] *SNOLAB*. https://www.snolab.ca. Accessed: 2017-06-06.

[21] E. Conti et al. "Correlated fluctuations between luminescence and ionization in liquid xenon". In: *Phys. Rev. B* 68 (5 2003), p. 054201. DOI: 10.1103/PhysRevB.68.054201.

[22] M. Agostini, G. Benato, and J. Detwiler. "Discovery probability of next-generation neutrinoless double-β decay experiments". In: (2017).

[23] H. Dautet et al. "Photon counting techniques with silicon avalanche photodiodes". In: *Appl. Opt.* 32.21 (1993), pp. 3894–3900. DOI: 10.1364/AO.32.003894.

[24] L. Fabris. "Novel Readout Design Criteria for SiPM-Based Radiation Detectors". PhD thesis. University of Bergamo, 2015.

[25] L. Fabris et al. *Concepts of SiPM readout electronics*. Workshop on large area, low background, VUV sensitive photo-detectors and associated electronics. IEEE Nuclear Science Symposium and Medical Imaging Conference. (Date last accessed 6-July-2015). [Online]. Available: http://info.ornl.gov/sites/publications/Files/Pub52995.pptx. 2014.

[26] S. Vinogradov. "Analytical models of probability distribution and excess noise factor of solid state photomultiplier signals with crosstalk". In: *Nuclear Instruments and Methods in Physics Research A* 695 (2012), pp. 247–251. DOI: 10.1016/j.nima.2011.11.086.

[27] A. Jamil. *Light Detection with SiPMs in the nEXO Experiment*. CPAD Instrumentation Frontier 2016: New Technologies for Discovery II. Accessed: 2017-06-06.

[28] R. Neilson. "Discovery of the Two-Neutrino Double-Beta Decay of Xenon-136 with EXO-200". PhD thesis. Stanford University, 2011.

[29] *Eckert and Ziegler*. http://www.ezag.com/home/. Accessed: 2017-06-16.

[30] *Pelham Research Optical*. http://www.pelhamresearchoptical.com. Accessed: 2017-06-19.

[31] *Thorlabs*. https://www.thorlabs.com. Accessed: 2017-06-17.

[32] *Pfeiffer*. https://www.pfeiffer-vacuum.com/en/. Accessed: 2017-06-17.

[33] *Omegal*. http://www.omega.com. Accessed: 2017-06-19.

[34] *CAEN*. http://www.caen.it. Accessed: 2017-06-19.

[35] *FBK*. https://www.fbk.eu/en/. Accessed: 2017-06-21.

[36] E. Bellamy et al. "Absolute calibration and monitoring of a spectrometric channel using a photomultiplier". In: *Nuclear Instruments and Methods in Physics Research Section A: Accelerators, Spectrometers, Detectors and Associated Equipment* 339.3 (1994), pp. 468–476. doi: http://dx.doi.org/10.1016/0168-9002(94)90183-X.

[37] *Institute of Microelectronics of Chinese Academy of Sciences*. http://english.ime.cas.cn. Accessed: 2017-06-28.

[38] D. E. Alburger and A. W. Sunyar. "Decay of Bi^{207}". In: *Phys. Rev.* 99 (3 1955), pp. 695–702. doi: 10.1103/PhysRev.99.695.

[39] *Eagle Steel*. https://eaglesteel.com/wp-content/uploads/2016/04/304_Stainless_Steel.pdf. Accessed: 2017-06-29.

[40] *LIGO Vacuum Compatible Materials List*. https://dcc.ligo.org/E960050/public. Accessed: 2017-06-30.

[41] *McMaster-Carr*. https://www.mcmaster.com. Accessed: 2017-06-30.

[42] *Mill-Max*. https://www.mill-max.com/support. Accessed: 2017-06-30.

[43] A. LaTorre and S. Seibert. *Fast Optical Monte Carlo Simulation With Surface-Based Geometries Using Chroma*. 2011.

Acknowledgements

I would like to thank all the persons, who have supported me throughout my life and my academic carrier, who helped me through my struggles and celebrated my successes:

- **Gisela Anton** for giving me the opportunity to work on such a great project and for her helping me to achieve my goals. Being able to go to Stanford and getting accepted at Yale would not have been possible without your guidance.
- **Thilo Michel** for being a great mentor, who shared so much of his experience with me and helped me become the scientist I am. You have advised me in every step I took ever since I started in your group.
- **Giorgio Gratta** for kindly hosting me in his group at Stanford. It was a pleasure working with so many outstanding people and get to know the Californian lifestyle.
- **Marcia Keating** for helping me out with everything since the first day I arrived at Stanford.
- **Jutta Dziwis** for her patience with all the mess I created and for all the little chats.
- **Alexis Schubert, Igor Ostrovskiy, Gaosong Li, Mike Jewel, Daniel Fudenberg, Manual Weber, David Moore, Chas Blakemore, Alex Rider and Ralph DeVoe** for welcoming me in the Gratta group from the first day, teaching me so many things and making me want an espresso everyday after lunch. Thanks for this great time!
- **nEXO and EXO-200 Collaborations** for being such a great community, which I am happy to be a part of.
- **Tobias Ziegler and Michael Wagenpfeil** for their great support in trying to find out every little secret about SiPMs, not only for this thesis.
- **Patrick Hufschmidt, Judith Schneider, Gerrit Wrede, Sebastian Schmidt and the whole nEXO group** for the great working environment and all the things we were able to accomplish together.
- **My wife** for always standing beside me and supporting me in every situation. Even if that means moving together to New Haven for my PhD.
- **My family** for allowing me to pursue my dreams, making my life easier and be there whenever I need them.

Statutory Declaration

I declare that I have developed and written the enclosed Master's Thesis completely by myself, and have not used sources or means without declaration in the text. Any thoughts from others or literal quotations are clearly marked. The Master's Thesis was not used in the same or in a similar version to achieve an academic grading or is being published elsewhere.

Erlangen, July 21, 2017 Ako Jamil